3-D seismic imaging of the D" region beneath the Cocos Plate

Michael S. Thorne[1], Thorne Lay[2], Edward J. Garnero[1], Gunnar Jahnke[3,4], Heiner Igel[3]

[1]*Department of Geological Sciences, Arizona State University, Tempe, AZ 85287-1404, USA. E-mail: mthorne@asu.edu*

[2]*Department of Earth Sciences, University of California Santa Cruz, Santa Cruz, CA 95064, USA.*

[3]*Department of Earth and Environmental Sciences, Ludwig Maximilians Universität, Theresienstrasse 41, 80333 Munich, Germany.*

[4]*now at: Federal Institute of Geosciences and Natural Resources, Stilleweg 2, 30655 Hanover, Germany.*

Accepted:
Received:
In original form:

Corresponding author: Michael Thorne
Phone: 480-965-7680
Fax: 480-965-8102
Email: mthorne@asu.edu

3-D seismic imaging of the D" region beneath the Cocos Plate

Michael S. Thorne[1], Thorne Lay[2], Edward J. Garnero[1], Gunnar Jahnke[3,4], Heiner Igel[3]

[1]*Department of Geological Sciences, Arizona State University, Tempe, AZ 85287-1404, USA. E-mail: mthorne@asu.edu*
[2]*Department of Earth Sciences, University of California Santa Cruz, Santa Cruz, CA 95064, USA.*
[3]*Department of Earth and Environmental Sciences, Ludwig Maximilians Universität, Theresienstrasse 41, 80333 Munich, Germany.*
[4]*now at: Federal Institute of Geosciences and Natural Resources, Stilleweg 2, 30655 Hanover, Germany.*

SUMMARY

We use a 3-D axi-symmetric finite difference algorithm to model *SH*-wave propagation through cross-sections of 3-D lower mantle models beneath the Cocos Plate derived from recent data analyses. Synthetic seismograms with dominant periods as short as 4 sec are computed for several models: (1) a D" reflector 264 km above the CMB with laterally varying *S*-wave velocity increases of 0.9% to 2.6%, based on localized structures from a 1-D double-array stacking method; (2) an undulating D" reflector with large topography and uniform velocity increase obtained using a 3-D migration method; and (3) cross-sections through the 3-D mantle *S*-wave velocity tomography model TXBW. We apply double-array stacking to assess model predictions of data. Of the models explored, the *S*-wave tomography model TXBW displays the best overall agreement with data. The undulating reflector produces a double *Scd* arrival that may be useful in future studies for distinguishing between D" volumetric heterogeneity and D" discontinuity topography. 3-D model predictions show waveform variability not observed in 1-D model predictions. It is challenging to predict 3-D structure based on localized 1-D models when lateral structural variations are on the order of a few wavelengths of the energy used, particularly for the grazing geometry of our data. Iterative approaches of computing 3-D

synthetic seismograms and adjusting 3-D model characteristics by considering path integral effects are necessary to accurately model fine-scale D" structure.

1 INTRODUCTION

1.1 Lower Mantle Discontinuities

Ever since the designation of the D" region (Bullen 1949), consisting of heterogeneous velocity structure in the lowermost 200-300 km of the mantle, researchers have sought to characterize the detailed nature of this boundary layer. The mechanisms responsible for D" heterogeneity, manifested in strong arrival time fluctuations of seismic phases sampling the region, are still poorly constrained. It is important to characterize the D" region because its role as a major internal thermal boundary layer of Earth affects many disciplines, including mineral physics, global geodynamics, geochemistry, and geomagnetism (see Lay *et al.* 2004a for a review). The existence of a D" shear velocity discontinuity, discovered by Lay & Helmberger (1983), has added further complexity to creating a detailed picture of the D" region.

Only a handful of seismological techniques directly detect the D" discontinuity. The discontinuity is most commonly detected by observations of a travel-time triplication in *S*- and/or *P*- waves bottoming in the lower mantle. The structure has also been detected by observations of a strong arrival in the coda of $PKKP_{AB}$ (Rost & Revenaugh 2003). Studies of differential travel times between pairs of seismic phases (e.g., *ScS-S*, *PcP-P,* $PKKP_{AB}$-$PKKP_{DF}$) support the presence of a relatively abrupt increase in deep mantle wave-speeds in the lowermost mantle (e.g., Creager & Jordan 1986; Woodward &

Masters 1991; Zhu & Wysession 1997). Although the differential travel time studies are compatible with a D" discontinuity, they do not resolve its presence.

During the past two decades, the D" discontinuity has been detected in numerous seismic investigations (see Wysession *et al.* 1998 for a review). These studies have characterized the D" discontinuity as being a sharp *P*- and/or *S*- wave velocity (V_P and/or V_S) increase (~0.5 to 3.0% for V_P and ~0.9 to 3.0% for V_S) ranging in height from 150 to 350 km above the core-mantle boundary (CMB) with an average height of 250 km.

The *P*-wave observations most convincingly associated with a D" discontinuity are for paths beneath northwestern Siberia (e.g., Weber & Davis 1990; Houard & Nataf 1993). Other studies using *P*-wave data fail to find strong evidence for the discontinuity at many locations (e.g., Ding & Helmberger 1997). However, a lack of observations of *P*-wave reflections does not necessarily indicate non-existence of a velocity increase in D". For example, the sharpness, or depth extent, of the boundary plays an important role in its reflectivity. At grazing angles, where the wavefield triplicates, a velocity increase spread out over roughly 100 km can match most triplication data as accurately as for a sharp discontinuity (e.g., Young & Lay 1987; Gaherty & Lay 1992). However; pre-critical and high-frequency *P*-waves will be only weakly reflected by such a gradient increase. An undulating boundary may produce intermittent reflections or scattering that confuse detections of reflections. Additionally, a relatively low amplitude V_P jump at the D" discontinuity appears to be common, yielding reflections below the detection limit of routine seismic techniques. In general, past studies have not established whether a D" *P*-wave velocity discontinuity is ubiquitous or intermittent.

In contrast, *S*-wave reflections from a D" discontinuity are more common. A number of studies have revealed three regions of the deep mantle where the existence of a D" *S*-wave velocity discontinuity is particularly well supported by *S*-wave observations. These three regions are:

1. Beneath Siberia (e.g., Lay & Helmberger 1983; Weber & Davis 1990; Gaherty & Lay 1992; Weber 1993; Garnero & Lay 1997; Valenzuela & Wysession 1998; Thomas et al. 2004b),
2. Beneath Alaska (e.g., Lay & Helmberger 1983; Young & Lay 1990; Lay & Young 1991; Kendall & Shearer 1994; Matzel et al. 1996; Garnero & Lay 1997; Lay et al. 1997), and
3. Beneath Central America (e.g., Lay & Helmberger 1983; Zhang & Lay 1984; Kendall & Shearer 1994; Kendall & Nangini 1996; Ding & Helmberger 1997; Reasoner & Revenaugh 1999; Ni *et al.* 2000; Garnero & Lay 2003; Lay *et al.* 2004b; Thomas *et al.* 2004a; Hutko *et al.* 2005).

Some locations in the deep mantle where seismic observations do not show evidence for a shear wave discontinuity are adjacent to regions where observations do indicate the presence of a discontinuity. Explanations of why the discontinuity may appear or disappear over small spatial scales (e.g., < 100 km Lay *et al.* 2004b) are still debated. Strong topographic relief on the discontinuity and/or rapid 3-D velocity variations beneath the discontinuity have been invoked as possible explanations (e.g., Kendall & Nangini 1996; Thomas *et al.* 2004a).

Additional studies using *S*-waves have shown evidence for the discontinuity beneath the Central Pacific (Garnero *et al.* 1993; Avants *et al.* 2004). This has motivated

speculation that the feature is global (e.g., Sidorin *et al.* 1999). Nevertheless, further probing of the deep mantle, especially under the Southern Pacific and Atlantic Ocean regions, is needed before the lateral extent of the feature can be ascertained.

1.2 S-wave Triplication Behavior

Because the D" discontinuity increase for V_S appears to be greater than for V_P, studies utilizing triplications in the *S*-wave field have been the preferred method for detecting the discontinuity. In this paper we restrict our attention to *S*-waves observed on transverse component (*SH*) recordings at epicentral distances ranging from roughly 70º to 85º. Fig. 1 shows synthetic *SH* displacement seismograms computed using a finite difference axi-symmetric method for SH-waves (SHaxi). This method is described in (Jahnke *et al.* 2005) and is used to compute synthetic seismograms for D" discontinuity models.

In Fig. 1 synthetic seismograms for the PREM (Dziewonski & Anderson 1981) shear velocity structure, which does not contain a D" discontinuity, are shown with dotted lines. Synthetic seismograms for a D" discontinuity model with a 1.3% V_S increase (relative to PREM) 264 km above the CMB are shown in black. Neither model has crustal layers, as discussed below. Synthetics for the discontinuity model exhibit a travel-time triplication with extra arrivals between *S* and *ScS*. We use the nomenclature of Lay & Helmberger (1983) to describe the triplication phases labeled in Fig 1. The direct *S*-wave turning above the discontinuity is termed *Sab* whereas the *S*-wave energy turning below the discontinuity is termed *Scd*. *Sbc* denotes arrivals reflecting off the discontinuity. The post-critical *Sbc* arrival is progressively phase shifted, producing a small negative overshoot of the combined *Scd* + *Sbc* arrival. In Fig. 1 distinct *Scd* and

Sbc arrivals are discernible at larger distances; however the *Scd* and *Sbc* arrivals are generally not separately distinguishable in broadband data. Hence, we refer to the combined (*Scd* + *Sbc*) arrival as *SdS*. Most studies reference *SdS* travel-times and amplitudes to *ScS* (also shown in Fig. 1). Because the synthetics shown in Fig. 1 were created for a 500 km deep source, the seismic phase *s400S*, an underside reflection from the 400 km discontinuity above the source, is also observed. The amplitude of *s400S* is usually too low to be observed in broadband data without stacking records (e.g., Flanagan & Shearer 1998).

Fig. 2 shows the ray path geometry of the seismic phases in Fig. 1 for a receiver at an epicentral distance of 75º. The ray path geometry is for the same discontinuity model used to create the synthetic seismograms in Fig. 1. Also shown in Fig. 2 is the *SH*-velocity wavefield at one instance in time through a cross-section of the Earth computed with the SHaxi method. The relationship between spherical wave fronts and geometrical rays, which are perpendicular to the wave fronts, can be seen. Infinite frequency ray paths are useful for visualizing the path that seismic energy takes through the mantle, however, the seismic energy interaction with Earth structure surrounding the geometric ray must be considered because it also contributes energy to the seismic phases recorded at the surface (e.g., Dahlen *et al.* 2000).

1.3 Study region and objectives

The D" discontinuity beneath the Central American region has been investigated extensively because of excellent data coverage provided by South American events and North American receivers. Three recent studies have focused on mapping the D" discontinuity structure in 3-D beneath the Cocos Plate subset of the Central American

region (Lay *et al.* 2004b; Thomas *et al.* 2004a; Hutko *et al.* 2005). A recent tomographic inversion including *SdS* arrivals has also imaged the lower 500 km of the mantle beneath Central America (Hung *et al.* 2005). These regional studies have produced models for the structure of the discontinuity in the Cocos Plate region and will be discussed in detail in Section 3.

The variability in seismic differential travel-time (e.g., *ScS-Scd* or *Scd-Sab* differential travel-times – referred to hereafter as $T_{ScS-Scd}$ and $T_{Scd-Sab}$ respectively) or amplitude ratio (e.g., *Scd*/S*cS*) observations relative to optimal 1-D model predictions indicates the presence of 3-D D" structure (e.g., Lay & Helmberger 1983; Kendall & Nangini 1996). Because D" discontinuity topography and V_S heterogeneity are both likely to be 3-D in nature (e.g., Tackley 2000; Farnetani & Samuel 2005), there are major challenges in resolving discontinuity topography from surrounding volumetric velocity heterogeneity. Moreover, many D" discontinuity structures have been inferred based on using localized 1-D processing techniques, without it being clear how to generalize those models to 3-D structures. This is particularly problematic for triplication arrivals that graze the deep mantle, with extensive horizontal averaging of the structure. 3-D models have been obtained using migration approaches that assume homogeneous reference structures and point-scattering assumptions, which intrinsically bias the model images. Tomography methods usually do not account for abrupt velocity discontinuities, and incur errors by incorrect back-projection of travel-times on incorrect raypaths.

In order to progress from 1-D processing and modeling techniques that use simplifying assumptions for 3-D modeling, seismologists must use advanced synthetic seismogram techniques. Numerical techniques for computing synthetic seismograms in 2-

or 3-D are now becoming practical because of the recent availability and processing power of cluster computing. In this paper, we produce 3-D synthetic seismograms for our versions of 3-D models based on various D" discontinuity modeling results beneath the Cocos Plate. We also create synthetic seismograms through cross-sections of a recent *S*-wave tomography models (Grand 2002). The models we construct and compute synthetics for are summarized in Table 1. We compare waveforms and travel-time differentials from the computed synthetic seismograms with each other and with broadband data used in the studies of Lay *et al.* (2004b) and Thomas *et al.* (2004a). Furthermore, we analyze the limits of using localized 1-D processing techniques and lateral interpolations to infer 3-D D" discontinuity structure.

2 3-D AXI-SYMMETRIC FINITE DIFFERENCE METHOD AND VERIFICATION

Constraining models of 3-D D" structure requires computation of synthetic seismograms for 3-D geometries (hereafter referred to as 3-D synthetic seismograms) for comparison to original data. This also allows an assessment of if and how localized 1-D modeling results or migration methods should be extrapolated to predict actual 3-D structure. We use the 3-D axi-symmetric finite difference method (SHaxi) (based after Igel & Weber 1995, 1996; and extended in Jahnke *et al.* 2005) to explore the 3-D model extrapolations based on recent models of heterogeneous D" structure beneath the Cocos Plate obtained from several distinct procedures. This is the first application of the SHaxi method to original data.

The SHaxi method does not incorporate full 3-D Earth models as in some other numerical techniques (e.g., the spectral element method of Komatitsch & Tromp 2002). Instead the model defined on a grid in the vertical plane containing the great circle arc is

expanded to 3-D by (virtually) rotating the grid around the vertical axis. As a consequence the computation on a 2-D grid provides seismogram with the correct geometrical spreading, but only for axi-symmetric geometries. Nonetheless, this axi-symmetric method has several advantages for computing synthetic seismograms. Because it computes the wave field on a 2-D grid, synthetic seismograms can be generated for much shorter dominant periods (e.g., down to 1 sec) than with full 3-D techniques. SHaxi also maintains the correct 3-D geometrical spreading, which is an advantage over purely 2-D techniques that do not.

The main restriction in using the SHaxi method is that structures incorporated on the 2-D axi-symmetric grid act as 3-D ring-like structures (see Jahnke *et al.* 2005). This makes it impossible to model focusing and defocusing effects due to variations off the great circle plane. Additionally the source acts as a strike-slip with a fixed SH source radiation pattern proportional to the sine of the takeoff angle. This fixed radiation pattern makes direct comparison of amplitudes between synthetics and data from arbitrary oriented sources slightly complicated. In this study we are primarily concerned with differential travel time effects and we place less emphasis on amplitude effects.

In order to produce synthetic seismograms at relatively high frequencies we used 16 nodes (128 processors) of the Hitachi SR8000 super computer at the Leibniz-Rechenzentrum, Munich, Germany. These computations require 42,000 (lateral) × 6,000 (radial) finite difference grid-points. This grid spacing corresponds to roughly 0.5 km between grid-points radially, and varies between 0.5 km (Earth's surface) and 0.25 km (CMB) laterally. Calculations are run to 1700.0 seconds of simulation time, which takes approximately 24 hours to compute. For these input parameters, synthetic seismograms

with a dominant period of 4 sec are produced. This is suitable for comparisons with our *SH* observations which have been low-pass filtered with a cut-off of 3.3 sec.

In order to ensure that our computations are accurate for the time and epicentral distance windows used in this study, we used the Gemini (Greens Function of the Earth by Minor Integration) method of Friederich & Dalkolmo (1995) to compute 1-D PREM synthetics for comparison to our finite-difference results. The window containing *Sab* and *ScS* that we use starts 20 sec before and ends 100 sec after the *Sab* arrival in epicentral distance ranging from 70º – 85º. The Gemini method was chosen because it has previously been used for verification of other synthetic seismogram techniques (Igel *et al.* 2000). We produced 10 sec dominant period synthetics with the Gemini method for use in our comparisons. Overlaying individual traces display excellent agreement between the SHaxi and Gemini methods, as demonstrated by a minimum cross-correlation coefficient between records of 0.9982 at 85º.

In synthetics created for PREM [Supplemental Fig. A], crustal and mid-crustal reverberations interfere with the *SdS* arrival. The average crustal structure represented in PREM is not a realistic estimate of the complex crustal structure beneath southern California recording stations (e.g., Zhu & Kanamori 2000). In order to compare our synthetics to data from southern California stations, we remove the crustal layers from PREM before computing synthetic seismograms.

3 STUDY REGION AND MODEL CONSTRUCTION

3.1 D" structure beneath the Cocos Plate

The D" discontinuity structure beneath the Cocos Plate region has been the focus of numerous seismological studies. Thomas *et al.* (2004a) provide a review of these

studies, finding that a D" *S*-wave velocity discontinuity has been consistently inferred at a height ranging between 150 – 300 km above the CMB with a velocity increase ranging from 0.9 – 3.0%. There is little evidence for a corresponding *P*-wave velocity D" discontinuity (e.g., Ding & Helmberger 1997; Rost, private communication, 2005) other than the work of Reasoner & Revenaugh (1999) who stack many short-period signals and infer a weak reflector (0.5 – 0.6% *P*-wave velocity increase) about 190 km above the CMB.

Five recent studies have attempted to assess possible small-scale 2- or 3-D variability of the D" discontinuity beneath the Cocos Plate. Lay *et al.* (2004b), Thomas *et al.* (2004a), and Hutko *et al.* (2005) produced D" discontinuity models for the Cocos Plate region using various stacking and migration methods. We compute synthetic seismograms through cross-sections of our 3-D constructions of the models produced by Lay *et al.* (2004b) and Thomas *et al.* (2004a). Ni *et al.* (2000) computed synthetic seismograms through cross-sections of the tomography model of Grand (1994) to determine whether that shear velocity structure helped to improve 1-D D" discontinuity models. We similarly compute synthetic seismograms for the most recent tomography model of Grand (2002) for comparison. Hung *et al.* (2005) presented a lower mantle tomography model of the Central American region that overlaps the Cocos Plate region. However, consideration of the Hung *et al.* (2005) model suggests that it lacks adequate data sampling in our study region and we do not analyze it further here. We summarize below how we produced model cross-sections for use in the SHaxi method, and the results of comparing data to the resulting 3-D synthetics.

3.2 Double-array stacking model

Lay *et al.* (2004b) analyzed broadband transverse component seismic seismograms including *SdS* and *ScS* arrivals from 14 deep South American events recorded by Californian regional networks. Fig. 3a shows the source-receiver geometries used. The study employed the double-array stacking technique of Revenaugh & Meyer (1997) to obtain apparent reflector depths of *SdS* energy for localized bins of data with nearby *ScS* CMB reflection points. Fig. 3b shows detailed outlines of the four geographic bins in which Lay *et al.* (2004b) grouped their data. *SdS* energy was detected in stacks throughout the region, however the area delimited by Bin 2 showed weak *SdS* energy and some individual seismic traces did not show clear *SdS* arrivals between *Sab* and *ScS*, as previously noted by Garnero & Lay (2003). If the shear velocity within the D" layer (i.e., between the D" discontinuity and the CMB) is laterally uniform, the stacks imply localized topography of the discontinuity ranging over 150 km, in which case the amplitude variations might arise due to reflection from an undulating reflector. However, Rokosky *et al.* (2004) and most mantle tomography models suggest a general south-to-north increase in D" V_S from Bin 1 to Bin 4, based primarily on *ScS* arrival times. Lay *et al.* (2004b) modeled the data using localized 1-D models, allowing the average velocity in the D" layer to vary as needed to match the amplitude of *SdS*. They found that the variations required to match the amplitude kept the depth of the discontinuity almost constant. Their final model involved a 264 km thick D" layer with varying V_S increase across the D" layer ranging from 0.9 to 2.6%. The resulting structures match the general trend of the *ScS* arrival time data, except for the model in Bin 1, which predicts earlier

ScS arrivals than observed. Reconciling the *SdS* amplitudes and *ScS* arrival times requires a model with a large discontinuity about 100 km deeper than in bins to the north.

To create models for use with the SHaxi method based on the localized 1-D results of Lay *et al*. (2004b), we construct cross-sections through four average great circle paths from source clusters to station clusters (Path 1 – Path 4, Fig. 3b). These great circle paths are based on the average event-receiver location for events that have *ScS* bounce-points in each of the four geographic bins. For each cross-section, we use PREM velocities above the D" discontinuity. A brief description of models and their naming convention are outlined in Table 1. We constructed models with two end-member scenarios: (1) the velocity structure in each bin is block-like (model LAYB) [Supplemental Fig. B]; and (2) the velocity structure is linearly interpolated between the center of each bin (model LAYL). We use the same great circle paths (Paths 1-4) to construct cross-sections for the models listed in Table 1. We note that this process assumes very localized sensitivity of the 1-D modeling as implied by the fine binning used; as found below this results in very small scale variations that are at odds with the intrinsic resolution of the nearly horizontally grazing ray geometry.

3.3 Point-scattering migration model

Thomas *et al.* (2004a) employed a pre-critical point-scattering migration technique (Thomas *et al.* 1999) to image the deep mantle beneath the Cocos Plate using the same data set as Lay *et al.* (2004b). The imaged model space was roughly 700 km in length and 150 km wide (study region T shown in Fig. 3b). The migration study used the 1-D background model ak135 (Kennett *et al.* 1995) to provide travel-times for stacking windows of seismogram subsets compatible with scattering from a specified 3-D grid of

scattering positions. V_S was not allowed to vary laterally, which projects all travel time variations into apparent scattering locations within the background model. A smoothed version of the resultant scattering image gives a topographically varying D" discontinuity surface with a south-to-north increase in discontinuity height above the CMB from 150 to 300 km. This apparent topography is similar to the double-array stacking results of Lay *et al.* (2004b) for a 1-D stacking model. The 150 km increase in discontinuity height occurs in the center of the image region (near Bin2 of Lay *et al.* (2004b)), over a lateral distance of roughly 200 km. The central region, containing the transition in discontinuity depth, does not reflect strong coherent energy and there is uncertainty in the continuity of the structure. The topography in this model is completely dependent on the assumption of 1-D background structure.

The migration approach used by Thomas *et al.* (2004a) does not model the amplitudes and like all Kirchhoff migrations, simply images a reflector embedded in the background model without accounting for wave interactions with the structure. In order to compute synthetic seismograms for this structure, it is necessary to prescribe the V_S increase across the imaged reflector. Previous 1-D modeling efforts for the region suggested a 2.75% (Lay & Helmberger 1983; Kendall & Nangini 1996) or 2.0% (Ding & Helmberger 1997) V_S increase, but Lay *et al.* (2004b) suggest the region has strong lateral variability ranging from 0.9 to 2.6%. As initial estimates, we chose V_S increases of 2.0% (model THOM2.0) and 1.0% (model THOM1.0).

Recent studies of a lower mantle phase transition from magnesium silicate perovskite to a post-perovskite (ppv) structure indicate that the phase transition should involve 1.5% V_S and 1% density increases (Tsuchiya *et al.* 2004a), providing a possible

explanation for the D" discontinuity. This phase transition also is predicted to have a steep Clapeyron slope of ~7-10 MPa K^{-1} (Oganov & Ono 2004; Tsuchiya *et al.* 2004b), which could account for significant topography on the D" discontinuity. Because the study of Thomas *et al.* (2004a) suggests rapidly varying topography, as may accompany a ppv phase transition in the presence of lateral thermal and compositional gradients (e.g., Hernlund *et al.* 2005), we also create synthetic seismograms with 1.5% V_S and 1% density increases (model THOM1.5). Model cross-sections are shown in Supplemental Fig. B for model THOM2.0.

3.4 Tomography model

A consistent feature of recent *S*-wave tomography models (e.g., Masters *et al.* 1996; Kuo *et al.* 2000; Megnin & Romanowicz 2000; Ritsema & van Heijst 2000; Gu *et al.* 2001; Grand 2002) is the presence of relatively high shear velocities beneath the Central America and Cocos Plate region. Model TXBW (parameterized with 2.5º × 2.5º bins – roughly 150 km on a side) from Grand (2002) was not developed using triplication arrivals and resolves longer wavelength structure than models produced by Lay *et al.* (2004b) and Thomas *et al.* (2004a). The reference model for TXBW has relatively high D" velocities, and the lowest layer (bottom 220 km of the mantle) in model TXBW contains high V_S perturbations (up to ~2.3% increases) relative to PREM beneath the Cocos Plate, with a general south-to-north velocity increase. This is consistent with the results of Lay *et al.* (2004b).

Ni *et al.* (2000) utilized the WKM method (a modification of the WKBJ method of Chapman 1978) to produce synthetic seismograms through 2-D cross-sections of block-style tomography models. As an application of their method, Ni *et al.* (2000)

produced synthetics through two cross-sections of Grand's (1994) tomography model, with great-circle paths passing through the Central American region. Ni *et al.* (2000) were not able to observe the *SdS* phase in Grand's model for the chosen great-circle paths without arbitrarily increasing the velocity perturbations in the lowermost layer of Grand's model by a factor of 3. Their synthetics then compare favorably to broadband *Scd* waveforms of Ding & Helmberger (1997) for the Cocos Plate region.

We created four cross-sections through Grand's most recent tomography model TXBW (Grand 2002) for synthetic seismogram construction with the SHaxi method. To create cross-sections, we mapped the heterogeneity in TXBW onto our finite difference grid using four-point inverse distance weighted interpolation between the V_S values given in the model. Our cross-section through great circle Path 1 (Fig. 3) is identical to one of the cross-sections used in the study of Ni *et al.* (2000).

Model TXBW is parameterized in layers of blocks with constant *S*-wave velocity perturbations (δV_S). We observe a noticeable increase in average V_S between the two lowermost layers along each of our reference great-circle paths (Path1: +1.5%; Path 2: +1.75%; Path 3: +1.75%; Path 4: +2.0% - Supplemental Fig. C). Ni *et al.* (2000) referenced the heterogeneity in Grand's tomography model directly to PREM (S. Ni, private communication, 2005) rather than to the 1-D reference model actually used in Grand's inversion. When we use the 1-D reference model of Grand, with its velocity increase in the lowermost mantle, the tomographic models produces significant *SdS* energy from the boundary between the two lowermost layers and we find no need to arbitrarily enhance the structure [Cross-sections are shown in Supplemental Fig. C and D]. Cross-sections through model TXBW show moderate variation in V_S progressing

between Paths 1-2-3-4. The strongest variation in velocity structure is observed between Path 1 and 4.

4 SYNTHETIC SEISMOGRAM RESULTS

We computed synthetic seismograms for each great-circle path through the three models described in the preceding section. Significant variability in waveform shape and differential travel-times between seismic phases is found in the synthetic seismograms for the various models, as we discuss below. We consider $T_{ScS\text{-}Scd}$ and $T_{ScS\text{–}Sab}$, *Scd*/*ScS* amplitude ratios, and waveform characteristics between the different predictions.

4.1 Models LAYB and LAYL

Synthetic seismograms were computed for models LAYB and LAYL which have block-like or linearly interpolated V_S structures, respectively. Differences in waveform shape or travel-time of arrivals between LAYB and LAYL are not observable for the 4-s dominant period of our synthetic seismograms. This is because the geographic bin size used by Lay *et al.* (2004b) is small compared with the wavelength of *S*-wave energy in the D" region (bins are ~2.5º wide in the great circle arc direction, or ~5 wavelengths of a 4 sec dominant period wave at the CMB). The effect of bin size on $T_{ScS\text{-}Scd}$ and $T_{ScS\text{-}Sab}$ will be discussed in Section 7.

We also compute synthetic seismograms for the 1-D models from Lay *et al*. (2004b) to compare with our synthetics for the 3-D interpolation of those models. Overlaying synthetics for model LAYB with synthetics for the 1-D models illuminates the 3-D structural effects on waveform shape and timing [Supplemental Fig. E]. 3-D synthetics for model LAYB show simple *SdS* waveforms, similar to the 1-D predictions, with $T_{Scd\text{-}Sab}$ between the 1-D and 3-D models unchanged. However, there exists large

variability in $T_{ScS-Scd}$ between the synthetics. This is not unexpected since *ScS* samples several bins in the 3-D computation, and thereby averages the laterally varying D" structure. For example, 3-D predictions for Path 2 of LAYB show reduced $T_{ScS-Scd}$ (~1.5 sec decrease for 70º-80º) from those for the optimal 1-D model for Bin 2. This discrepancy is due to *ScS* having its central bounce-point in Bin 2 (with a 0.4% V_S increase in the 1-D model), but the *ScS* wave also travels through Bins 1 and 3 (which have 0.9% and 0.7% V_S increases throughout D", respectively). Thus the 3-D $T_{ScS-Scd}$ is relatively reduced, since *ScS* is advanced by the neighboring bins. Path 3 similarly has a smaller $T_{ScS-Scd}$ (~1.5 sec decrease). This illustrates the challenge of how to interpret a suite of localized 1-D model results; the models need to be projected and averaged along the ray paths in a manner akin to tomography when constructing a 3-D model rather than being treated as local blocks as we have done

In addition to the large variations between 1-D and 3-D predicted $T_{ScS-Scd}$ significant variations in *Scd*/*ScS* amplitude ratios are present. Only minor discrepancies exist in predicted *ScS*/*Sab* amplitude ratios implying that differences in 1-D and 3-D *Scd/ScS* predictions are due to 3-D effects on *Scd*. In general, increasing V_S below the D" discontinuity increases *Scd* amplitudes. *Scd* amplitudes in the 3-D synthetics are sensitive to D" velocities in the neighboring bins because of the grazing ray geometry and the large resultant Fresnel zone. For example, synthetics for Path 2 of LAYB show an increase in the *Scd*/*ScS* amplitude ratio over synthetics for the 1-D Bin 2 model (ratio increase from 0.07 to 0.15), owing to Bin 2 being juxtaposed with two higher velocity bins. This suggests that mapping of localized 1-D structure into a 3-D model requires

attention to the effective Fresnel zone as well. This is intrinsic to migration and finite-frequency tomography approaches.

4.2 Models THOM1.0, THOM1.5, and THOM2.0

We constructed three models based on Thomas *et al.* (2004a), one for each of three distinct D" velocities (see Table 1). Larger D" velocity increases produce smaller $T_{ScS\text{-}Scd}$ and larger *Scd/ScS* amplitude ratios, which accounts for the main differences in synthetics for models THOM1.0, THOM1.5, and THOM2.0. Model THOM1.5 also included a 1% density increase, which produced indistinguishable synthetics from those either lacking or containing greater density increases (up to 5%).

Although differences between models THOM1.0 – THOM2.0 are straightforward, *ScS-Scd* differential timing and *Scd*/*ScS* amplitude ratio effects between Paths 1-4 are complex [Supplemental Fig. F]. Here, we restrict the discussion on variable Path effect to model THOM2.0.

Along Path 1, the wavefield encounters the deepest D" discontinuity (~130 km above the CMB) (see Supplemental Fig. B). Consequently, $T_{ScS\text{-}Scd}$ are the smallest. Along Path 4, the wavefield encounters the shallowest D" discontinuity (~290 km above the CMB). Although $T_{ScS\text{-}Scd}$ for Path 4 are greater than for Path 1 (ranging between 1.5 sec larger at 80º to 9 sec larger at 71º), the largest $T_{ScS\text{-}Scd}$ are sometimes observed for paths 2 and 3. Along Paths 2 and 3 the wave field encounters the transition from a deep to shallow D" discontinuity. Three snapshots of the *SdS* and *ScS* energy are shown for Path 3 (Fig. 4), which displays the development of a double *Scd* arrival. In Fig. 4(a) as the wave field interacts with the deepest D" discontinuity structure the *Scd* phase is already apparent. 50 sec later the wavefield interacts with the transition from a deep to

shallow discontinuity (Fig. 4b), showing more *Scd* complexity due to multipathing with the shallower and deeper discontinuities. A double *Scd* arrival is fully developed 50 sec later, apparent as two distinct *Scd* peaks in the synthetic seismograms.

At closer epicentral distances (from 70º-72º for Path 3) the *Scd* arrival originating from the deeper discontinuity contains higher amplitudes. At the further epicentral distances (> 72º for path 3) the *Scd* arrival originating from the shallower discontinuity contains the higher amplitudes. Arrival times based on *Scd* peak amplitudes imply an abrupt jump in $T_{ScS\text{-}Scd}$ at the epicentral distance where *Scd* amplitudes from the shallower discontinuity overtake *Scd* amplitudes from the deeper discontinuity. For Path 3 a 3 sec change in $T_{ScS\text{-}Scd}$ occurs at 72º.

4.3 Model TXBW

Fig. 5 shows overlain synthetic seismograms computed for model TXBW for Paths 1 and 4. A clear *SdS* arrival between *Sab* and *ScS*, as well as arrivals between *Sab* and *SdS* caused by crustal reverberations, are apparent for both models. Because of the layered block-style inversion used to create TXBW, other small arrivals are present from discontinuous jumps between layers.

Decreases in $T_{ScS\text{-}Sab}$ (generally < 1 sec on average, but up to 2 sec between paths 1 and 4) are observed moving from Path 1 to 4, due to progressively increasing V_S toward the north in the D" region. This also decreases $T_{ScS\text{-}Scd}$ (by <1 sec on average between Path 1 and 4). 3-D structure elsewhere along the paths likely plays an important role in timing and amplitude anomalies (e.g., Zhao & Lei 2004), but our focus here is on D" structure. Nonetheless, we note variable *Scd/ScS* amplitude ratios that are not easily understandable in terms of D" structure alone.

5 SYNTHETIC SEISMOGRAMS COMPARED WITH DATA

The most direct assessment of a model's performance is to compare the synthetic predictions with data. We compare synthetic predictions for Path 1 with the data set used in the studies of Lay *et al.* (2004b) and Thomas *et al.* (2004a). The four Bins used by Lay *et al.* (2004b) contained records spanning limited epicentral distance ranges. The ranges are: Bin 1: 79º-82º; Bin 2: 71º-79º; Bin 3: 75º-82º; Bin 4: 70º-77º. It is difficult to detect *SdS* in individual records for epicentral distances less than roughly 78º, because *Scd* amplitudes are relatively low at shorter distances and are often obscured by noise in the traces. The inferred small D" discontinuity V_S increase (e.g., 0.4% for Bin 2, or 0.7% for Bin 3) also makes detection of *SdS* energy in individual traces problematic. These two factors make direct comparison of data with synthetics challenging for Paths 2, 3, and 4. Data grouped into Bin 1 show *SdS* energy in individual traces, allowing us to compare these recordings with synthetic seismograms for Path 1.

Fig. 6 shows synthetics seismograms for models LAYB, THOM1.5, THOM2.0 and TXBW along with data from the April 23, 2000, Argentina event. Although some scatter exists in travel-times and amplitudes of *SdS* energy for signals grouped into Bin 1, the event shown in Fig. 6 is representative. As previously mentioned, the SHaxi method has a fixed source radiation pattern, so amplitude differences in the phases shown in Fig. 6 are not exactly comparable, with the synthetics expected to show relatively low *ScS/Sab* amplitude ratios due to the effective source radiation pattern.

Model LAYB (Fig. 6a) adequately explains $T_{ScS\text{-}Scd}$, although $T_{ScS\text{-}Sab}$ are slightly too long. Model THOM1.0 (not shown in Fig. 6) reproduces $T_{ScS\text{-}Scd}$ the best amongst the models based on Thomas *et al*. (2004a) but does predict $T_{ScS\text{-}Scd}$ as well as model LAYB.

Model THOM1.5 (Fig. 6b) performs better than model THOM2.0 in reproducing $T_{ScS\text{-}Scd}$; however, model THOM1.5 does worse than THOM2.0 in predicting the $T_{ScS\text{-}Sab}$ differential times. Model THOM2.0 (Fig. 6c) predicts $T_{ScS\text{-}Sab}$ differential times accurately, but under-predicts $T_{ScS\text{-}Scd}$ by as much as 2.5 sec. The best agreement between synthetics and data for Path 1 is observed for model TXBW (Fig. 6d). $T_{ScS\text{-}Sab}$ and $T_{ScS\text{-}Scd}$ are in excellent agreement particularly for distances greater than ~80º. TXBW slightly over-predicts $T_{ScS\text{-}Sab}$ for distances less than 80º, however, $T_{ScS\text{-}Scd}$ is well matched.

6 DOUBLE-ARRAY STACKING COMPARISONS

Because it is difficult to observe the *Scd* phase in individual records for distances less than 78º, the studies of Lay *et al.* (2004b) and Thomas *et al.* (2004a) employed data stacking techniques to infer D" discontinuity properties. Here we stack synthetic seismograms using the double-array stacking technique of Revenaugh & Meyer (1997) to obtain apparent reflector depths of the *SdS* energy (as in Lay *et al.* 2004b). The SHaxi method has a fixed source radiation pattern, and we can predict its effect on the amplitudes of resulting stacks. All that is needed is to slightly scale *ScS* relative to *SdS* in the stacking of synthetics by normalizing *ScS* in the synthetics on a value less than unity by an amount corresponding to the ratio of the radiation pattern coefficient for *ScS* divided by that for *SdS*. The actual data are not scaled for source radiation pattern because for each bin the average *SdS/ScS* corrections are very close to 1.0.

Fig. 7 shows double-array stacks of data compared to synthetic predictions, as functions of target depth relative to the CMB. PREM is used as the reference stacking velocity model for both data and synthetics, so apparent *SdS* reflector depths are biased to the same extent. We stack synthetics for ranges of epicentral distances that correspond to

those of the corresponding data. *ScS* energy stacks coherently at the CMB, because the *ScS* peaks are aligned on the reference *ScS* arrival times. *SdS* energy is clearly apparent in the data stacks at the apparent depths indicated by the arrows. Saw tooth irregularities at shallower depths occur as a result of individual waveform truncation before the *Sab* arrival. This is done because there tends to be a rise in amplitude of the traces in the *Sab* coda.

Double-beam stacking results are summarized in Table 2. Model THOM1.0 predicts the D" discontinuity height best, however, it under predicts the *SdS/ScS* amplitude ratio most severely. Overall, models LAYB and TXBW predict apparent D" discontinuity height and *SdS/ScS* amplitude ratios the best. Model THOM2.0 often predicts the *SdS/ScS* amplitude ratio as well as models LAYB and TXBW, but it under predicts the discontinuity height the most, and the *SdS* waveform shapes are irregular. None of the matches are as good as for the 1-D models for each bin obtained by Lay *et al.* (2004b).

Although synthetics for model TXBW compare well with data, the fit is not perfect, especially for Path 2 (Fig. 7). D" V_S likely varies on shorter scale lengths than TXBW is able to resolve, as suggested by the short-scale velocity variation of Lay *et al.* (2004b). It may be possible to obtain better synthetic-data agreement by slightly modifying model TXBW. The models of Lay *et al.* (2004b) may guide the direction such enhancements take, however, we found no simple procedure to map the structures suggested by Lay *et al.* (2004b) onto TXBW. Significant trial-and-error forward modeling, guided by the 1-D stacking results and the spatial distribution of the

tomography model appears to be the best way to formulate the search for a best-fitting model.

The stacks shown in Fig. 7(a) are in agreement with the results of comparing individual synthetics to data records as in Fig. 6. That is, we can see that model TXBW indicates a reflector at the same height above CMB as the data, while model LAYB suggests the height above CMB to be slightly higher than the data suggest. The LAYB result can be understood in that the model produced a slight over-prediction of the *ScS-Scd* differential travel-times. The under-predicted *ScS-Scd* differential travel-times of models THOM1.0-THOM2.0 are manifested in the stacks of Fig. 7(a) as deeper D" discontinuity reflectors than what these data suggest.

7 DISCUSSION

In this paper, we presented 3-D synthetic seismograms for recent models of deep mantle *S*-wave tomography and D" discontinuity structure beneath the Cocos Plate region. We compared these synthetics with broadband data. Our main focus has been to assess how well the 3-D models inferred from various analysis procedures actually account for the original observations. In this section, we discuss important sources of uncertainty and difficulties associated with the models for which we computed synthetic seismograms.

Lay *et al.* (2004b) produced 1-D models of the D" discontinuity structure with excellent agreement to data stacks. However, our 3-D synthetics for model LAYB compared less favorably to data stacks. The main issue here is how best to develop a 3-D structure from the 'local' characterization provided by small bin processing given the grazing nature of the seismic waves which must laterally average the structure. The *SdS*

features in the data stacks are remarkably discrete; even small overlap of the bins leads to appearance of double peaks in the stacks, as noted by Lay *et al.* (2004b). But the grazing ray geometry argues that this cannot be interpreted as resolving spatial heterogeneities on the scale of the actual binning. What is needed is an understanding of the mapping of the locally characterized wavefield into heterogeneous structure. This is undoubtedly a non-linear mapping given that volumetric heterogeneity and reflector topography can trade-off.

We explore the effects of V_S heterogeneity wavelength on $T_{ScS\text{-}Scd}$ and $T_{ScS\text{-}Sab}$ in Fig. 8. We construct a suite of models with a base model containing a D" discontinuity at a height of 264 km above the CMB and a V_S increase of 2.33%. Synthetic seismograms are computed for a source 500 km deep at an epicentral distance of 78º. The *ScS* bounce-point for this source-receiver geometry is located at 38.12º from the source. Centered on this *ScS* bounce-point we introduce a domain with higher V_S (+3% increase). This higher velocity domain is given a width along the great-circle path in varying multiples of the *ScS* wavelength for a dominant period of 7 sec (1 wavelength ≈ 50 km). In Fig. 8, the *ScS-Sab* differential travel times are shown as a function of domain size for the high velocity region. For $T_{ScS\text{-}Sab}$, a domain width of 2-3 wavelengths already affects the differential travel-times by a few tenths of seconds. However it is not until a domain width of roughly 30 wavelengths (~1500 km for a 7 sec dominant period wave) is reached that $T_{ScS\text{-}Sab}$ converges to the travel-time prediction for a 1-D model with a 3.0% V_S increase beneath the discontinuity. This is consistent with the long path length of *ScS* within the D" layer and the large effective Fresnel zone for wide-angle reflections as indicated in Figure 2.

The Bin sizes used in the Lay *et al.* (2004b) study are on average roughly 3 wavelengths in length along the great circle path. Fig. 8 demonstrates that differential travel-times may be significantly dominated by the neighboring bin structure. *ScS-Scd* times suffer a similar lack of path isolation. These experiments argue that 1-D travel time modeling results are biased if along path lateral variability is shorter scale than about 30-wavelengths. However, our *SdS* data clearly display strong variation over distances of much less than 30-wavelengths, thus 3-D techniques must be employed to reliably map the required heterogeneous structure. It is unrealistically optimistic to believe that fine binning resolves fine scale structure when grazing rays are being used; the wave propagation effects may be spatially rapidly varying but the responsible structure is likely to be large scale. Since tomography intrinsically distributes path integral effects over large scale, it can provide a good starting basis for initial modeling, as demonstrated by Ni *et al*. (2000) and by the modeling in this paper.

We also calculated $T_{ScS\text{-}Sab}$ and $T_{ScS\text{-}Scd}$ using 3-D ray tracing for the same model geometries as used for Fig. 8. The 3-D ray tracing solutions coincide with the travel-times shown in Fig. 8 to within a couple tenths of seconds. However, significant variations between ray tracing and waveform predictions occur when imaging low-velocity layers.

Paths 2 and 3 of models THOM1.0-2.0 show a rapid transition in D" discontinuity thickness (e.g., Fig 4 and Supplemental Fig. B) producing a double *Scd* peak in the synthetic predictions. This double *Scd* peak has not been reported in observations, but comes to light with the calculation of 3-D synthetic seismograms. Given the possibility of the post-perovskite phase transition being responsible for the D" discontinuity, it is

interesting to establish whether models with rapid variations in topography can account for the data. Future efforts seeking to resolve topographic variation on the D" discontinuity should consider the prediction of a double *Scd* arrival.

For the SHaxi approach, out of great circle plane variations in D" discontinuity topography cannot be modeled, so we do not model the exact scattering of energy that the full 3-D model of Thomas *et al.* (2004a) would produce. Because our models are axi-symmetric more *SdS* energy may be backscattered from the transition from thin to thick D" layering in models THOM1.0-2.0 than would be scattered in fully 3-D models. Models THOM1.0-2.0 have relatively small *SdS*/*Scd* amplitudes, though we are not able to constrain the degree of *Scd* amplitude misfit due to our geometry. Perhaps the greatest challenge for interpreting migration images is that they do not resolve velocity contrasts (at least for Kirchhoff point-scattering migrations), and the reflector images are highly dependent on the reference velocity structure. Volumetric heterogeneity as needed to match *ScS* arrival times suggests that apparent topography is likely to be incorrect, and in this case, exaggerated. Thus, the poor agreement of resulting synthetics is not a clear indication that the models are flawed; the mapping to 3-D may simply be in significant error. This uncertainty extends to any effort to infer dynamical features based on the migration images.

If V_S gradients perpendicular to our 2-D cross-sections for model TXBW are insignificant for a couple of wavelengths our synthetics should be adequate. Because there was only slight change in our synthetic predictions between individual paths, lateral variation does appears to be minor for our geometry and full 3-D synthetics may not be necessary to predict the waveforms. Not having to compute full 3-D synthetics for the

present class of whole Earth tomography models would drastically save computational resources and time, and is currently feasible using low-cost cluster computing. We are currently exploring differences between synthetics computed for tomography models with fully 3-D codes and the SHaxi method, which will be reported on soon.

8 CONCLUSIONS

We have demonstrated that important 3-D wavefield effects are predicted for models of 3-D structure built upon underlying 1-D modeling assumptions. We have investigated recent models of D" discontinuity structure beneath the Cocos Plate region using 3-D synthetic seismograms calculated with the finite-difference SHaxi method. We made synthetic predictions for 3-D models inferred from results of several recent "high resolution" imaging studies, including D" discontinuity mapping by stacking and migration, and tomographically derived volumetric heterogeneity. We focused our comparison on seismic phases predominantly used to image D" discontinuity structure: *S*, *ScS* and the intermediate arrival *SdS* which is present if a high velocity D" layer exists. We found significant discrepancies between observations and 3-D synthetic predictions, which highlight the need for 3-D tools in the process of mapping localized imaging results into 3-D structure. 1-D tools are unable to accurately predict 3-D structure if structural variations are on the order of wavelength of the energy used; the problem is particularly severe for grazing ray geometries. 3-D ray tracing techniques may aid in constructing 3-D models by providing improved reference seismic arrival times. However, methods utilizing 3-D synthetic seismograms, such as the SHaxi approach, are better suited for this purpose as important waveform effects can be synthesized. In order to model fine-scale 3-D D" structure, we believe future efforts should incorporate

methods of synthesizing 3-D seismograms in an iterative approach. Reasonable starting models may be constructed by migration or double-array stacking techniques, which may be improved if tomographic models are used as the reference structure. Initial models can be improved in an iterative fashion by computing 3-D synthetic seismograms, comparing the synthetics with data, and adjusting the model. However, it will be challenging to determine the best way to adjust the model in the forward sense, requiring significant trial and error. In the inverse sense, low cost methods such as SHaxi may allow reasonable full waveform inversions to be calculated along corridors densely sampled with data.

Acknowledgements

Most figures were generated using the Generic Mapping Tools freeware package (Wessel & Smith 1998). M. T. and E. G. were partially supported by NSF grant EAR-0135119. T. L. was supported by NSF Grant EAR-0125595. Thanks to the Leibniz Computing Center, Munich, for access to their computational facilities. Support is also acknowledged from the German Academic Exchange Service (IQN-Georisk), the German Research Foundation, and the Human Resources and Mobility Programme of the European Union (SPICE-Project). The SHaxi source code is openly available at http://www.spice-rtn.org/.

References

Avants, M. S., Lay, T. & Garnero, E., 2004. Imaging lower mantle structure beneath the Central Pacific by stacking S wave data, *EOS Trans. AGU*, **85**, Fall Meet. Suppl., Abstract T11E-1320.

Bullen, K. E., 1949. Compressibility-pressure hypothesis and the Earth's interior, *Monthly Notes of the Royal Astronomical Society*, Geophysics Supplement, 355-368.

Chapman, C.H., 1978. A new method for computing synthetic seismograms, *Geophys. J. R. astr. Soc.* **54**: 481-518.

Creager, K. C. & Jordan, T. H., 1986. Aspherical structure of the core-mantle boundary from PKP Travel-Times, *Geophysical Research Letters*, **13**, 1497-1500.

Dahlen, F. A., Hung, S. H. & Nolet, G., 2000. Frechet kernels for finite-frequency traveltimes - I. Theory, *Geophysical Journal International*, **141**, 157-174.

Ding, X. M. & Helmberger, D. V., 1997. Modelling D" structure beneath Central America with broadband seismic data, *Physics of the Earth and Planetary Interiors*, **101**, 245-270.

Dziewonski, A. M. & Anderson, D. L., 1981. Preliminary Reference Earth Model, *Physics of the Earth and Planetary Interiors*, **25**, 297-356.

Farnetani, C. G., and H. Samuel, 2005. Beyond the thermal plume paradigm, *Geophys. Res. Lett.*, 32, No.7, L07311, 10.1029/2005GL022360.

Flanagan, M. P. & Shearer, P. M., 1998. Topography on the 410-km seismic velocity discontinuity near subduction zones from stacking of sS, sP, and pP precursors, *Journal of Geophysical Research-Solid Earth*, **103**, 21165-21182.

Friederich, W. & Dalkolmo, J., 1995. Complete synthetic seismograms for a spherically symmetrical Earth by a numerical computation of the Greens-function in the frequency-domain, *Geophysical Journal International*, **122**, 537-550.

Gaherty, J. B. & Lay, T., 1992. Investigation of laterally heterogeneous shear velocity structure in D" beneath Eurasia, *Journal of Geophysical Research-Solid Earth*, **97**, 417-435.

Garnero, E. J., Helmberger, D. V. & Grand, S., 1993. Preliminary evidence for a lower mantle shear-wave velocity discontinuity beneath the Central Pacific, *Physics of the Earth and Planetary Interiors*, **79**, 335-347.

Garnero, E. J. & Lay, T., 1997. Lateral variations in lowermost mantle shear wave anisotropy beneath the north Pacific and Alaska, *Journal of Geophysical Research-Solid Earth*, **102**, 8121-8135.

Garnero, E. J. & Lay, T., 2003. D " shear velocity heterogeneity, anisotropy and discontinuity structure beneath the Caribbean and Central America, *Physics of the Earth and Planetary Interiors*, **140**, 219-242.

Grand, S. P., 1994. Mantle shear structure beneath the America and surrounding oceans, *Journal of Geophysical Research-Solid Earth*, **99**, 11591-11621.

Grand, S. P., 2002. Mantle shear-wave tomography and the fate of subducted slabs, *Philosophical Transactions of the Royal Society of London Series a-Mathematical Physical and Engineering Sciences*, **360**, 2475-2491.

Gu, Y. J., Dziewonski, A. M., Su, W. J. & Ekstrom, G., 2001. Models of the mantle shear velocity and discontinuities in the pattern of lateral heterogeneities, *Journal of Geophysical Research-Solid Earth*, **106**, 11169-11199.

Hernlund, J.W, C. Thomas, P.J. Tackley, A doubling of the post-perovskite phase boundary and structure of the Earth's lowermost mantle, *Nature*, 434, 883-886, 2005.

Houard, S. & Nataf, H. C., 1993. Laterally varying reflector at the top of D" beneath Northern Siberia, *Geophysical Journal International*, **115**, 168-182.

Hung, S.-H., Garnero, E., Chiao, L.-Y., Lay, T. & Kuo, B. Y., 2005. Finite frequency tomography of D" shear velocity heterogeneity beneath the Caribbean, *Journal of Geophysical Research*, **110**, doi: 10.1029/2004JB003373.

Hutko, A., Lay, T., Garnero, E. & Revenaugh, J. R., 2005. A folded slab at the core-mantle boundary beneath the Cocos Plate imaged by Kirchoff migration, *Nature*, submitted.

Igel, H. & Weber, M., 1995. SH-wave propagation in the whole mantle using high-order finite differences, *Geophys. Res. Let.*, 22, 731-734.

Igel, H. & Weber, M., 1996. P-SV wave propagation in the Earth's mantle using finite differences: Application to heterogeneous lowermost mantle structure, *Geophys. Res. Let.*, 23, 415-418.

Igel, H., Takeuchi, N., Geller, R. J., Megnin, C., Bunge, H. P., Clevede, E., Dalkolmo, J. & Romanowicz, B., 2000. The COSY Project: verification of global seismic modeling algorithms, *Physics of the Earth and Planetary Interiors*, **119**, 3-23.

Jahnke, G., M. S. Thorne, H. Igel, 2005. Global SH wave propagation with an axi-symmetric finite-difference scheme, *Geophysical Journal International*, submitted.

Kendall, J. M. & Shearer, P. M., 1994. Lateral Variations in D" thickness from long-period shear-wave data, *Journal of Geophysical Research-Solid Earth*, **99**, 11575-11590.

Kendall, J. M. & Nangini, C., 1996. Lateral variations in D" below the Caribbean, *Geophysical Research Letters*, **23**, 399-402.

Kennett, B. L. N., Engdahl, E. R. & Buland, R., 1995. Constraints on seismic velocities in the Earth from travel-times, *Geophysical Journal International*, **122**, 108-124.

Komatitsch, D. & Tromp, J., 2002. Spectral-element simulations of global seismic wave propagation - I. Validation, *Geophysical Journal International*, **149**, 390-412.

Kuo, B. Y., Garnero, E. J. & Lay, T., 2000. Tomographic inversion of S-SKS times for shear velocity heterogeneity in D ": Degree 12 and hybrid models, *Journal of Geophysical Research-Solid Earth*, **105**, 28139-28157.

Lay, T. & Helmberger, D. V., 1983. A lower mantle S-wave triplication and the shear velocity structure of D", *Geophysical Journal of the Royal Astronomical Society*, **75**, 799-837.

Lay, T. & Young, C. J., 1991. Analysis of seismic SV waves in the core's penumbra, *Geophysical Research Letters*, **18**, 1373-1376.

Lay, T., Garnero, E. J., Young, C. J. & Gaherty, J. B., 1997. Scale lengths of shear velocity heterogeneity at the base of the mantle from S wave differential travel times, *Journal of Geophysical Research-Solid Earth*, **102**, 9887-9909.

Lay, T., Garnero, E. J. & William, Q., 2004a. Partial melting in a thermo-chemical boundary layer at the base of the mantle, *Physics of the Earth and Planetary Interiors*, **146**, 441-467.

Lay, T., Garnero, E. J. & Russell, S. A., 2004b. Lateral variation of the D " discontinuity beneath the Cocos Plate, *Geophysical Research Letters*, **31**, doi:10.1029/2004GL020300.

Masters, G., Johnson, S., Laske, G. & Bolton, H., 1996. A shear-velocity model of the mantle, *Philosophical Transactions of the Royal Society of London Series a-Mathematical Physical and Engineering Sciences*, **354**, 1385-1410.

Matzel, E., Sen, M. K. & Grand, S. P., 1996. Evidence for anisotropy in the deep mantle beneath Alaska, *Geophysical Research Letters*, **23**, 2417-2420.

Megnin, C. & Romanowicz, B., 2000. The three-dimensional shear velocity structure of the mantle from the inversion of body, surface and higher-mode waveforms, *Geophysical Journal International*, **143**, 709-728.

Ni, S. D., Ding, X. M. & Helmberger, D. V., 2000. Constructing synthetics from deep earth tomographic models, *Geophysical Journal International*, **140**, 71-82.

Oganov, A. R. & Ono, S., 2004. Theoretical and experimental evidence for a post-perovskite phase of MgSiO3 in Earth's D " layer, *Nature*, **430**, 445-448.

Reasoner, C. & Revenaugh, J., 1999. Short-period P wave constraints on D " reflectivity, *Journal of Geophysical Research-Solid Earth*, **104**, 955-961.

Revenaugh, J. & Meyer, R., 1997. Seismic evidence of partial melt within a possibly ubiquitous low-velocity layer at the base of the mantle, *Science*, **277**, 670-673.

Ritsema, J. & van Heijst, H.-J., 2000. Seismic imaging of structural heterogeneity in Earth's mantle: Evidence for Large-Scale Mantle Flow, *Science Progress*, **83**, 243-259.

Rokosky, J. M., Lay, T., Garnero, E. J. & Russell, S. A., 2004. High-resolution investigation of shear wave anisotropy in D " beneath the Cocos Plate, *Geophysical Research Letters*, **31**, L07605.

Rost, S. & Revenaugh, J., 2003. Detection of a D " discontinuity in the south Atlantic using PKKP, *Geophysical Research Letters*, **30**, 1840.

Sidorin, I., Gurnis, M., & Helmberger, D. V., 1999. Evidence for a ubiquitous seismic discontinuity at the base of the mantle, Science, *286*, 1326-1331.

Tackley, P.J., 2000. Mantle convection and plate tectonics: Towards an integrated physical and chemical theory, *Science*, 288, 2002-2007, 2000.

Thomas, C., Weber, M., Wicks, C. W. & Scherbaum, F., 1999. Small scatterers in the lower mantle observed at German broadband arrays, *Journal of Geophysical Research-Solid Earth*, **104**, 15073-15088.

Thomas, C., Garnero, E. J. & Lay, T., 2004a. High-resolution imaging of lowermost mantle structure under the Cocos plate, *Journal of Geophysical Research-Solid Earth*, **109**, doi:10.1029/2004JB003013.

Thomas, C., Kendall, J., Lowman, J., 2004b. Lower-mantle seismic discontinuities and the thermal morphology of subducted slabs, *Earth Planet. Sci. Lett.*, **225**, 105–113.

Tsuchiya, T., Tsuchiya, J., Umemoto, K. & Wentzcovitch, R. A., 2004a. Phase transition in MgSiO3 perovskite in the earth's lower mantle, *Earth and Planetary Science Letters*, **224**, 241-248.

Tsuchiya, T., Tsuchiya, J., Umemoto, K. & Wentzcovitch, R. M., 2004b. Elasticity of post-perovskite MgSiO3, *Geophysical Research Letters*, **31**, L14603, doi:10.1029/2004GL020278.

Valenzuela, R. W. & Wysession, M. E., 1998. Illuminating the Base of the Mantle with Diffracted Waves, *in The Core-Mantle Boundary Region*, pp. 57-71, ed., Gurnis, M., Wysession, M. E., Knittle, E. & Buffet, B. A., American Geophysical Union, Washington, D.C.

Weber, M. & Davis, J. P., 1990. Evidence of a laterally variable lower mantle structure from P-waves and S-waves, *Geophysical Journal International*, **102**, 231-255.

Weber, M., 1993. P-wave and S-wave reflections from anomalies in the lowermost mantle, *Geophysical Journal International*, **115**, 183-210.

Wessel, P., and W. H. F. Smith, 1998. New, improved version of the Generic Mapping Tools released, *Eos Trans. AGU*, 79, 579.

Woodward, R. L. & Masters, G., 1991. Lower-mantle structure from ScS-S differential travel-times, *Nature*, **352**, 231-233.

Wysession, M. E., Lay, T., Revenaugh, J., Williams, Q., Garnero, E., Jeanloz, R. & Kellogg, L. H., 1998. The D" discontinuity and its implications, *in The Core-Mantle Boundary Region*, pp. 273-297, ed., Gurnis, M., Wysession, M. E., Knittle, E. & Buffet, B. A., American Geophysical Union, Washington, D.C.

Young, C. J. & Lay, T., 1987. Evidence for a shear velocity discontinuity in the lower mantle beneath India and the Indian-Ocean, *Physics of the Earth and Planetary Interiors*, **49**, 37-53.

Young, C. J. and T. Lay (1990). Multiple phase analysis of the shear velocity structure in the D" region beneath Alaska, *J. Geophys. Res.*, 95, 17385-17402.

Zhang, J. J. & Lay, T., 1984. Investigation of a lower mantle shear-wave triplication using a broad-band array, *Geophysical Research Letters*, **11**, 620-623.

Zhao, D. & Lei, J., 2004. Seismic ray path variations in a 3D global velocity model, *Physics of the Earth and Planetary Interiors*, **141**, 153-166.

Zhu, A. N. & Wysession, M. E., 1997. Mapping global D" P velocities from ISC PcP-P differential travel times, *Physics of the Earth and Planetary Interiors*, **99**, 69-82.

Zhu, L. P. & Kanamori, H., 2000. Moho depth variation in southern California from teleseismic receiver functions, *Journal of Geophysical Research-Solid Earth*, **105**, 2969-2980.

Figure Legends

Figure 1. Transverse component displacement synthetics are shown for a 500 km deep event at teleseismic ranges. The calculation is done for a D" discontinuity model with a 1.3% V_S increase located 264 km above the CMB (solid lines), and synthetics for PREM (dashed lines). Synthetics are aligned and normalized to unity on the phase *S*, and calculated for a dominant period of 4 sec. Phase labels are given for the D" model, noting that the PREM model does not display the triplication phase *SdS*. Note, the phase *SdS* is composed of the two arrivals *Scd* (positive peak) and *Sbc* (positive and negative peak immediately following *Scd*).

Figure 2. a) The *SH*- velocity wave field is shown at propagation time of 600 sec for a 500 km deep event with dominant source period of 6 sec. Selected wave fronts are labeled with black double-sided arrows. Ray paths are drawn in black for an epicentral distance of 75º. The calculation is done for the D" discontinuity (indicated with a dashed green line) model of Fig. 1. Non-linear scaling was applied to the wavefield amplitudes to magnify lower amplitude phases. b) Detail of wavefield shown in panel a. The region displayed is indicated by a dashed blue box in panel a.

Figure 3. Location of study region. Panel a) shows the general location of the study region. Shown are events (stars), receivers (triangles) event-receiver great circle paths

(dashed lines) and *ScS* bounce-points (circles) used in the studies of Lay *et al.* (2004b) and Thomas *et al.* (2004a). *ScS* bounce-points are calculated from the PREM model. Both studies utilize the same data set. Panel b) displays a detailed section of the study region. This panel shows the *ScS* bounce-points as white circles. 1-D models were produced in the study of Lay *et al.* (2004b) for 4 distinct bins outlined in this plot by black rectangles (labeled Bins 1-4). The dashed gray lines (labeled Paths 1-4) represent the average great circle paths of source-receiver pairs for these four Bins, and are also the Paths for which we calculate synthetics in this study. The dashed gray rectangle (labeled with a gray-shaded T) represents the area modeled in the study of Thomas *et al.* (2004a).

Figure 4. Snapshots at three time intervals are shown for model THOM2.0 for Path 3. The view displayed includes a section of the lower-most mantle between radii 3480 - 4500 km and between epicentral distances 25º - 55º. The amplitude of the *SH*- velocity wavefield is shown in red and blue. The top of the D" discontinuity in model THOM2.0 is drawn with a solid black line. Select seismic phases are labeled with double-sided arrows. These snapshots show the evolution of the wave field as it encounters a D" discontinuity with topographic variation. The topographic variation is observed to produce two distinct *Scd* arrivals.

Figure 5. Comparison of synthetics for model TXBW for Paths 1 (black) and 4 (gray). Transverse component displacement synthetics are shown. Synthetics are aligned and normalized to unity on the phase *Sab*, and calculated for a dominant period of 4 sec. For clarity, lines are drawn at the peak *SdS* and *ScS* arrival time for Path 1.

Figure 6. Comparison of synthetics created for Path 1 (solid lines) with data (dashed lines, April 23, 2000 Argentina 600 km deep event). Transverse component displacement synthetics and data are shown. Data are distance shifted to a source depth of 500 km. Approximate arrival times (peak amplitude) for the phases *Sab*, *Scd*, and *ScS* for data are indicated by solid lines so that differences between data and synthetic differential travel-times can be easily inspected visually. Receiver names are listed to the right of data traces.

Figure 7. Stacking results for each Path (1-4) of synthetic prediction and Bin (1-4) of data are shown. Data stacks from Lay *et al.* (2004b) are drawn in black. The epicentral distance range of these data is displayed in the upper right corner of each panel. We stacked synthetic seismograms for the same epicentral distance range as these data.

Figure 8. 3-D effects of D" lateral V_S heterogeneity on $T_{ScS-Sab}$ (panel a) and $T_{ScS-Scd}$ (panel b) is shown. These differential travel-times are computed for a D" model with a constant V_S = 7.375 km/sec (+2.33% jump) except in a box centered on the *ScS* bounce point for source-receiver epicentral distance of 78º and source depth of 500 km (central bounce-point = 38.12º). Inside this box the V_S is 7.431 km/sec (+3% jump). The D" thickness is fixed at 264 km corresponding with the study of Lay *et al.* (2004b). The width of the inner box is shown on the right axis in km and on the left axis in multiples of the wavelength of *ScS* in the box. The wavelength multiples are shown for a *ScS* dominant period of 7 sec for which the synthetics were computed.

Tables

Table 1. Models

Model	Description	Model based on:
LAYB[a]	Block style bins	Lay *et al.* 2004b
LAYL[a]	Linear interpolation between bins	Lay *et al.* 2004b
THOM1.0[b]	1% Vs increase beneath discontinuity	Thomas *et al.* 2004a
THOM1.5[b]	1.5% Vs & 1% ρ increase beneath discontinuity	Thomas *et al.* 2004a
THOM2.0[b]	2% Vs increase beneath discontinuity	Thomas *et al.* 2004a
TXBW	Tomographically derived δV_S heterogeneity	Grand 2002

[a]Fixed D" thickness, variable D" δV_S
[b]Variable D" thickness, fixed D" δV_S

Table 2. D" thickness (km)* from double-beam stacking for data and models

Path	Data	LAYB	THOM1.0	THOM1.5	THOM2.0	TXBW
Path 1	160	185	115	95	80	167
Path 2	270	227	234	215	200	210
Path 3	250	196	230	202	182	198
Path 4	220	229	213	193	172	199

*Thickness refers to *Scd* peak in Fig. 7.

Supplemental Figure Legends

Supplement A. Transverse component displacement synthetics are shown. Synthetics for PREM with a 500 km source depth are drawn in blue. Synthetics are aligned and normalized to unity on the phase *S*, and calculated for a dominant period of 4 sec.

Crustal and mid-crustal phases that interfere with the *SdS* and *ScS* wavefield are labeled with green lines. *S* and *ScS* are labeled with red lines. The yellow line labels the underside reflection of the 400 km depth discontinuity in PREM ($s^{400}S$).

Supplement B. Lower mantle cross-sections for a) 1-D D" discontinuity models of Lay *et al.* (2004b), b) model LAYB, and c) model THOM2.0. Cross-sections for each of the four Paths we computed synthetic seismograms for are shown. Color scaling is based on absolute V_S in each model.

Supplement C. a) Lower mantle cross-sections for model TXBW. Cross-sections for each of the four Paths we computed synthetic seismograms for are shown. Color scaling is based on V_S. b) V_S profile in the lower mantle through model TXBW. Shown is the 1-D V_S profile at an epicentral distance of 40º. This distance is chosen as approximating the central bounce point of *ScS* recorded at an epicentral distance of 80º. The profile is shown for Paths 1-4. Layer 20-22 refers to the number of layer in the tomographic inversion of Grand (2002). The phase *SdS* observes an effective D" discontinuity as indicated.

Supplement D. Whole mantle cross-sections for model TXBW. Cross-sections for each of the four Paths we computed synthetic seismograms for are shown. Color scaling is based on δV_S. Ray path geometry is shown for the phases *S* and *ScS* for a 500 km deep event (green star) recorded at receivers (green triangles) with epicentral distances 70º, 75º, 80º, and 85º.

Supplement E. Comparison of synthetics computed for the 1-D D" models of Lay *et al.* (2004b, drawn in gray) with synthetics created for model LAYB (drawn in black). Each panel displays synthetics for the labeled Path. Synthetics are aligned and normalized to unity on the phase *S*, and calculated for a dominant period of 4 sec.

Supplement F. Comparison of synthetics computed for models THOM1.5 (drawn in gray) and THOM2.0 (drawn in black). Each panel displays synthetics for the labeled Path. Synthetics are aligned and normalized to unity on the phase *S*, and calculated for a dominant period of 5 sec.

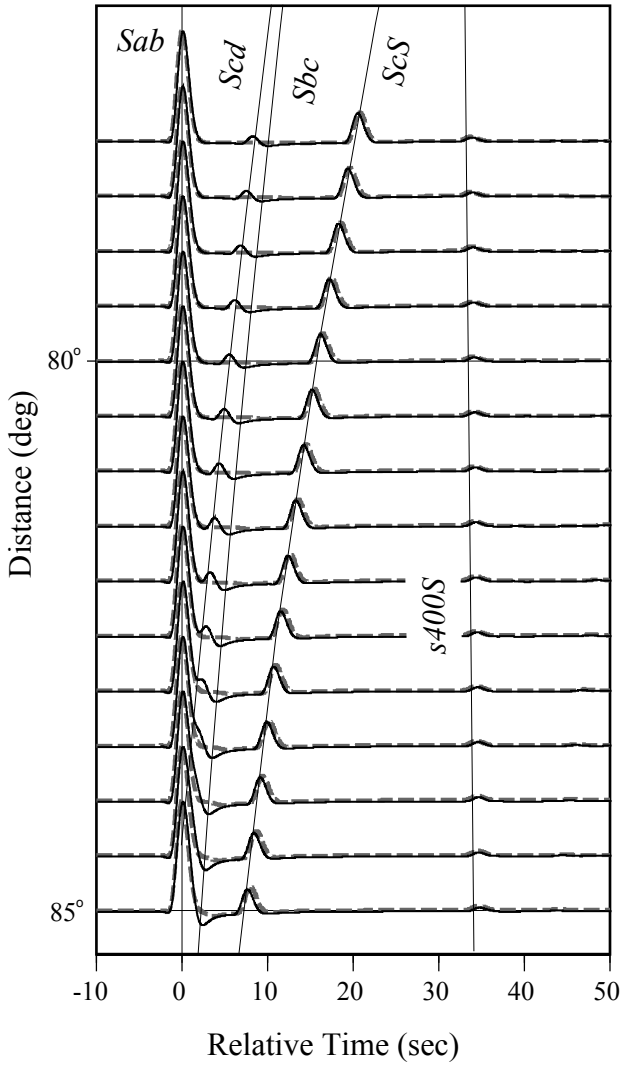

(Thorne, Lay, Garnero, Jahnke, and Igel. 2005)

(Span one column; Black and White)

Figure 1.

a) Wavefield and Ray Geometry

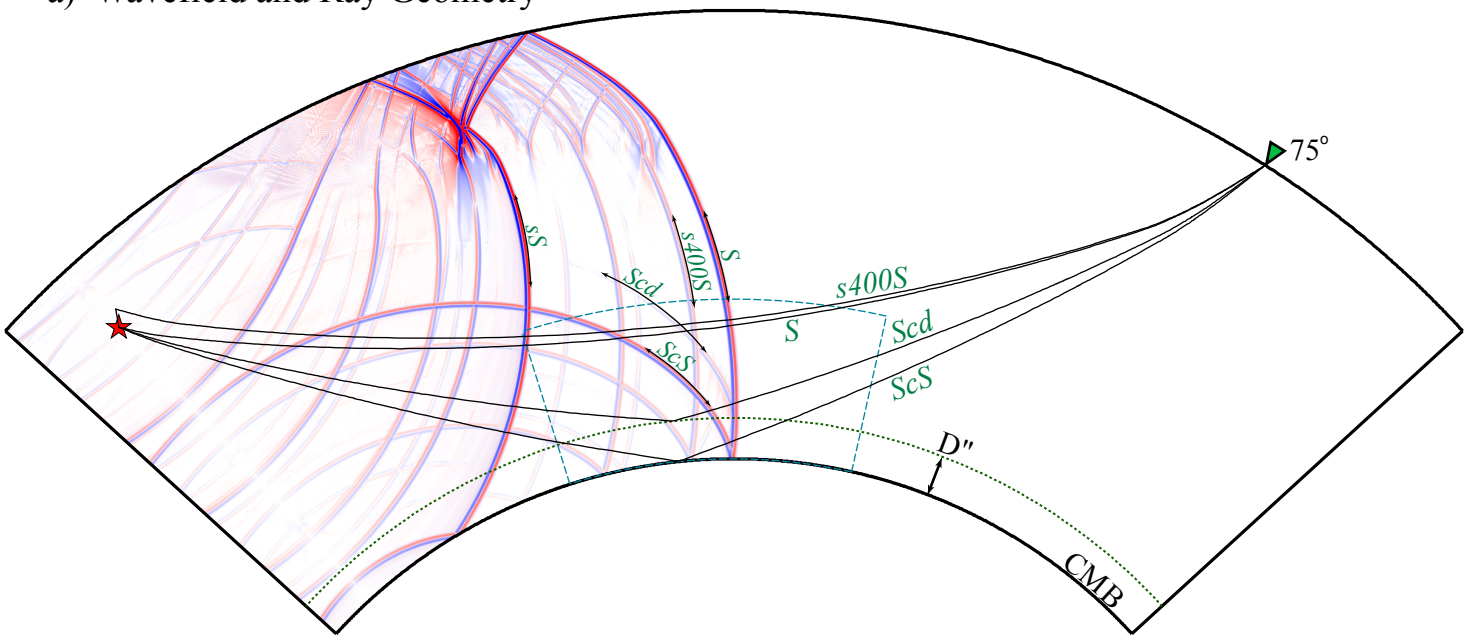

b) Wavefield and Ray Geometry - Detail

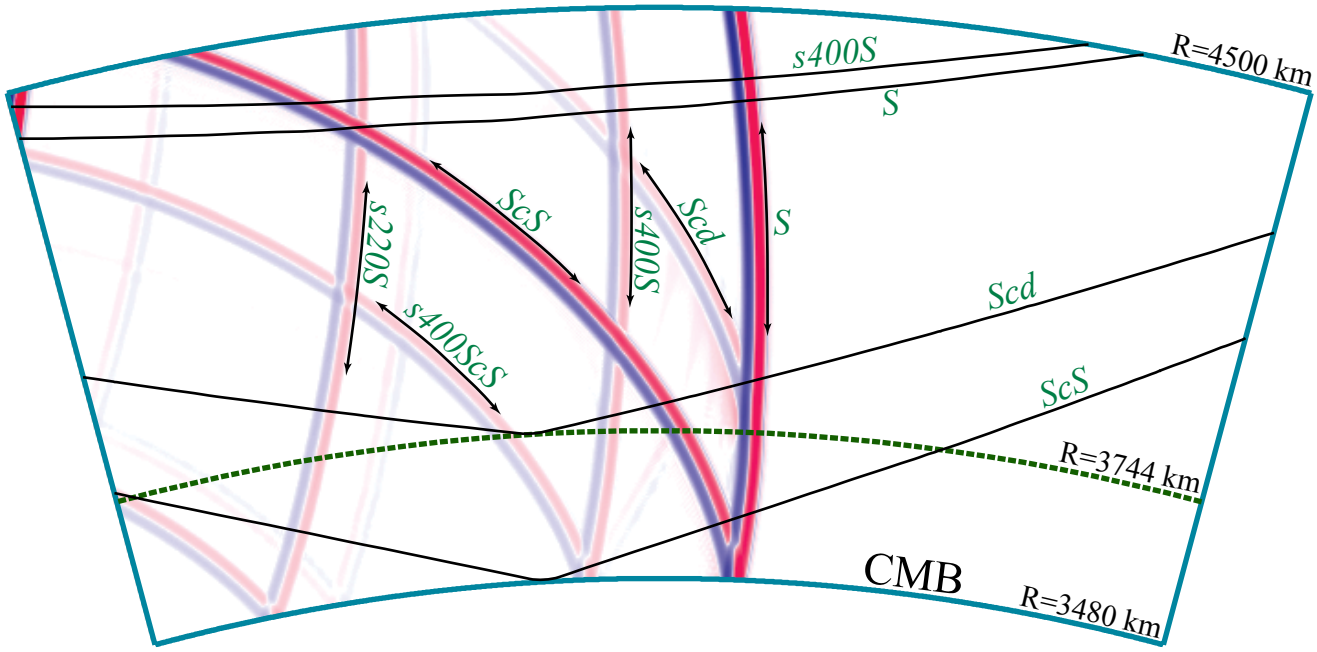

(Thorne, Lay, Garnero, Jahnke, and Igel. 2005)

(Span two columns; Color)

Figure 2.

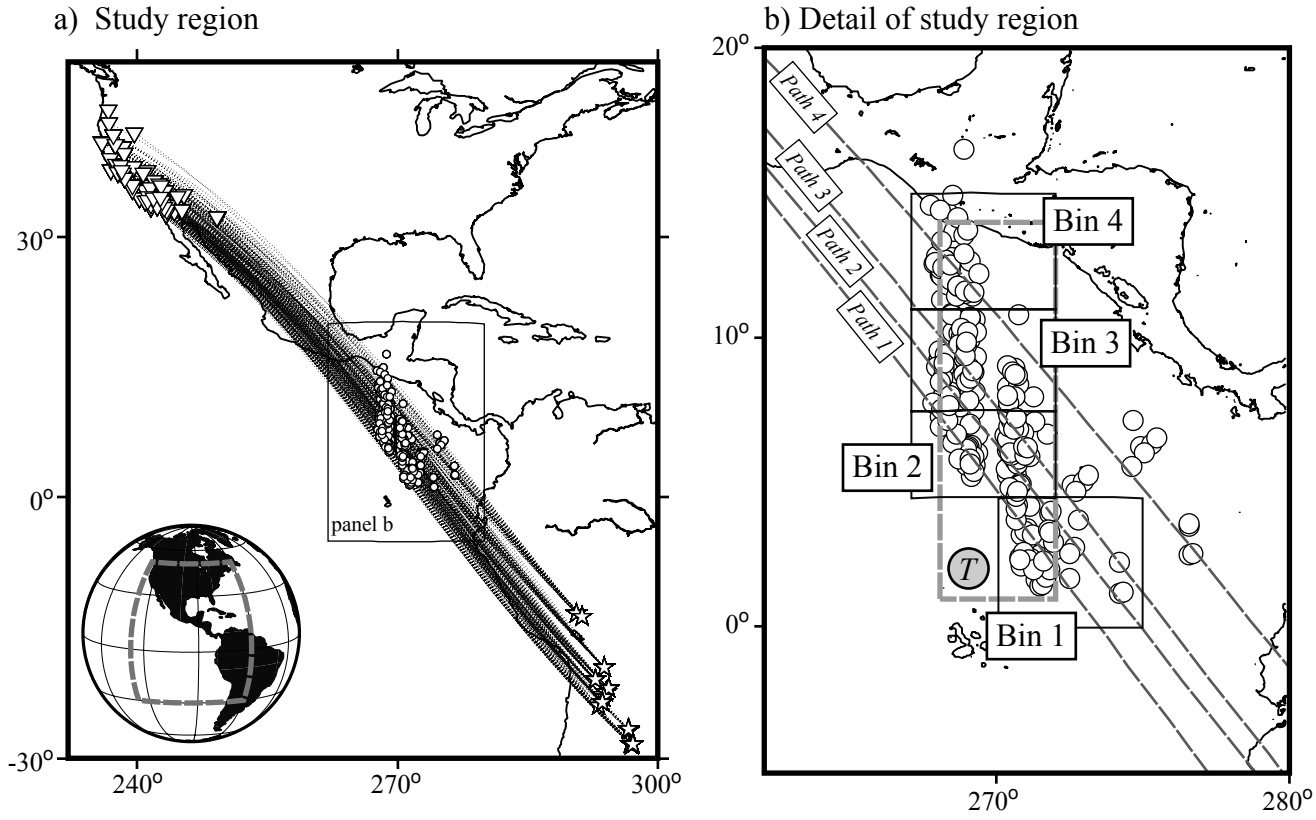

(Thorne, Lay, Garnero, Jahnke, and Igel. 2005)

(Span two columns; Black and White)

Figure 3.

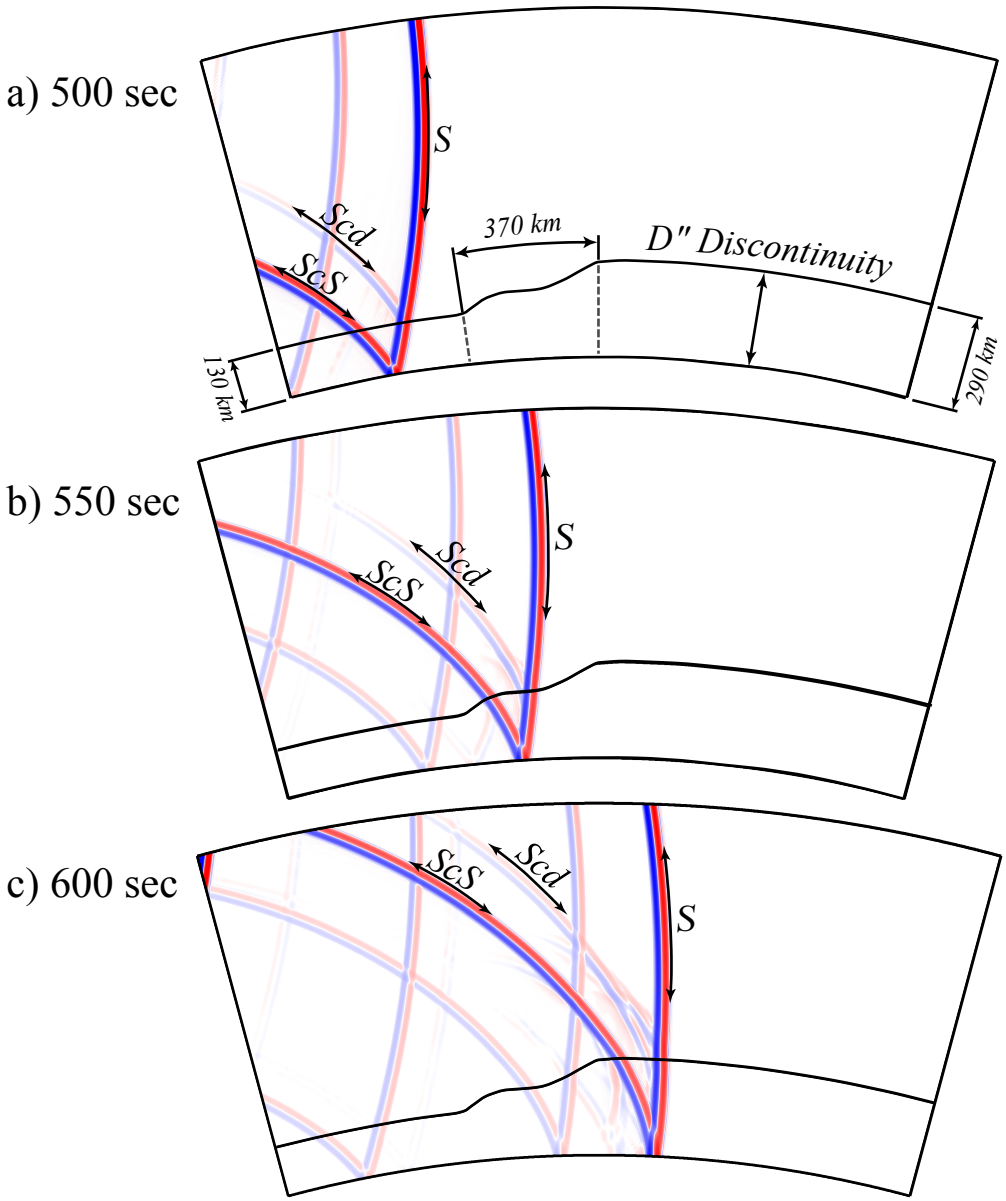

(Thorne, Lay, Garnero, Jahnke, and Igel. 2005)

(Span one column, color)

Figure 4.

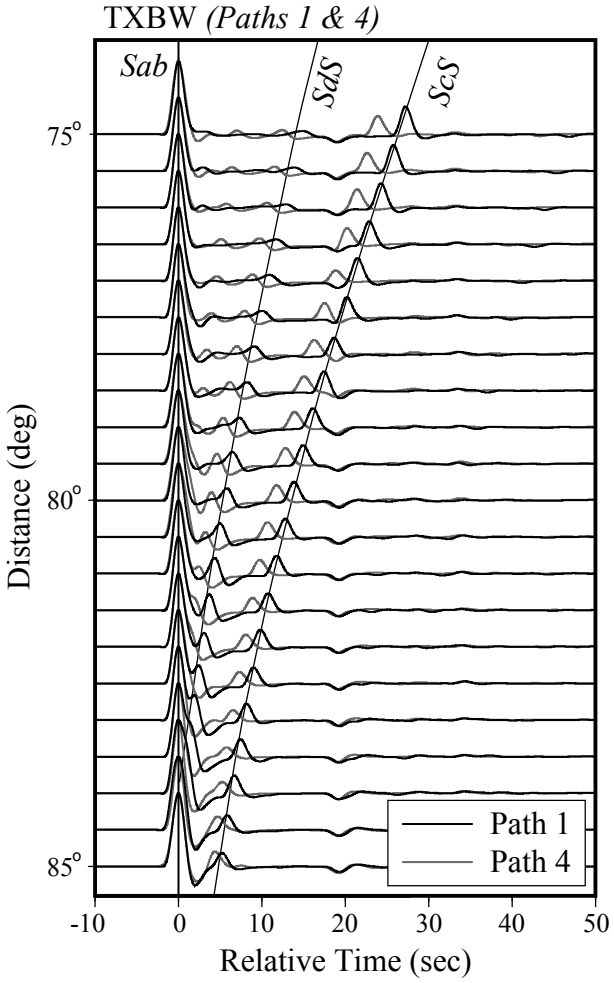

(Thorne, Lay, Garnero, Jahnke, and Igel. 2005)

(span one column; Black and White)

Figure 5.

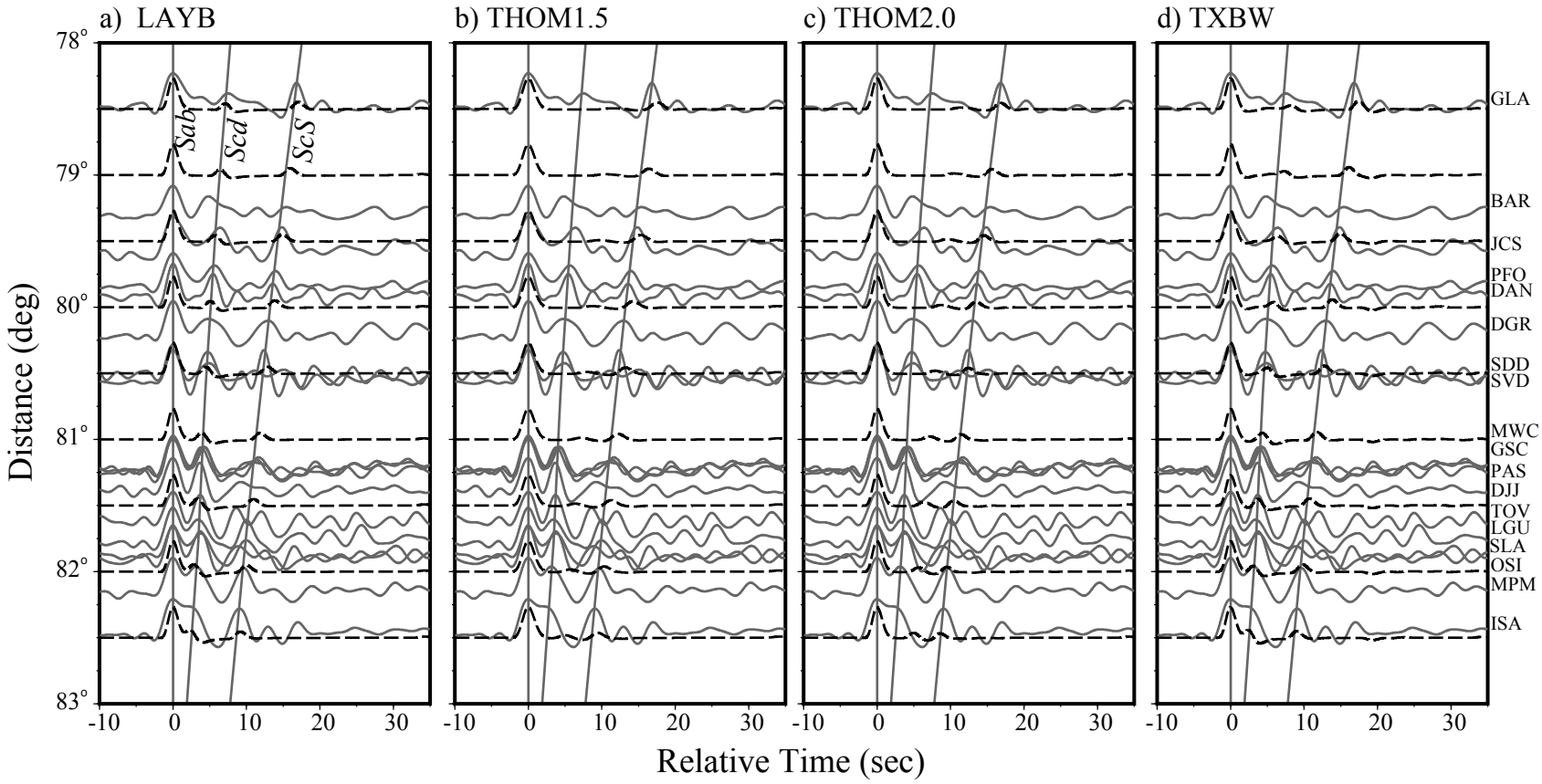

(Thorne, Lay, Garnero, Jahnke, and Igel. 2005)

(span two columns; Black and White)

Figure 6.

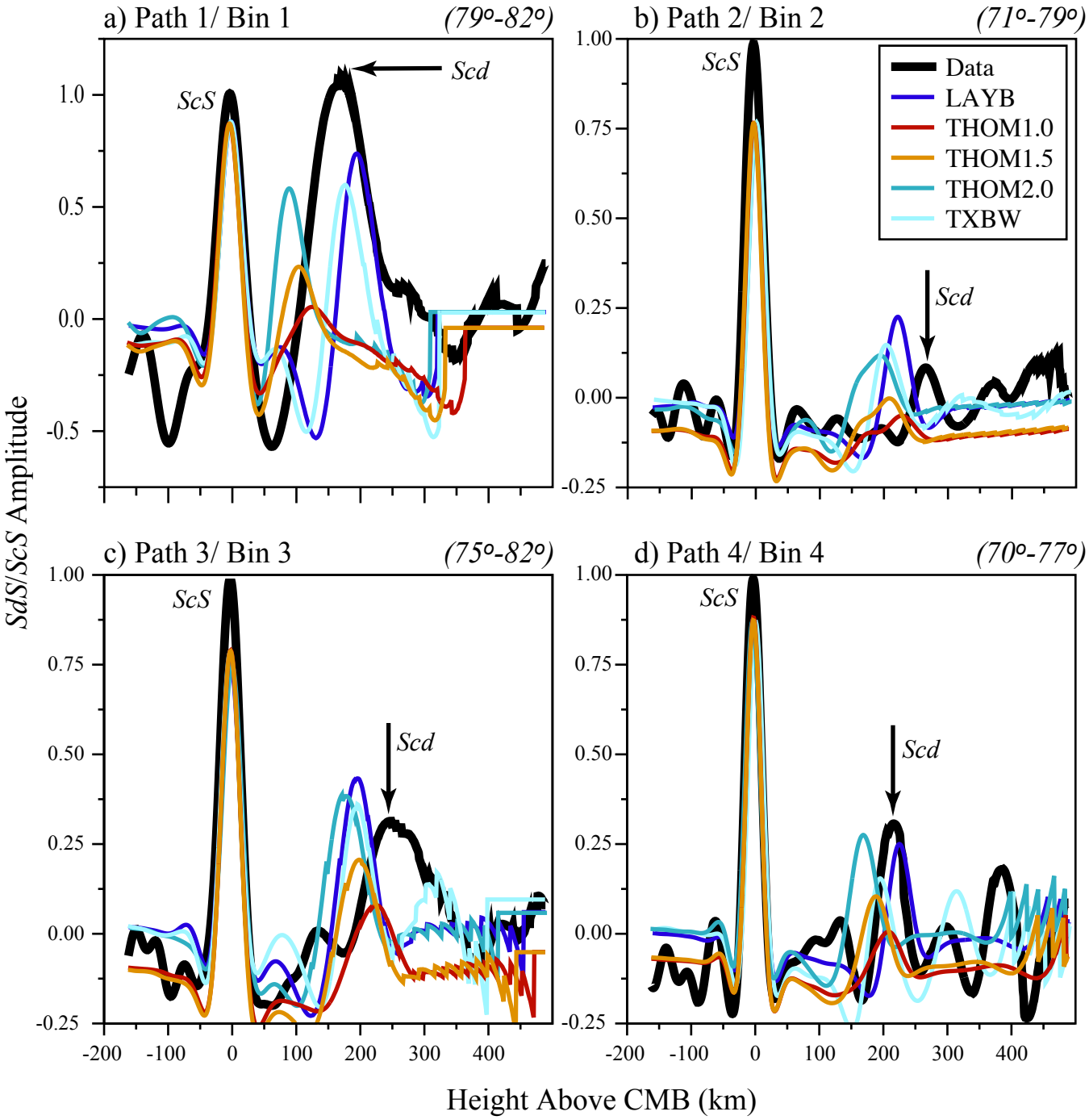

(Thorne, Lay, Garnero, Jahnke, and Igel. 2005)

(span two columns; Color)

Figure 7.

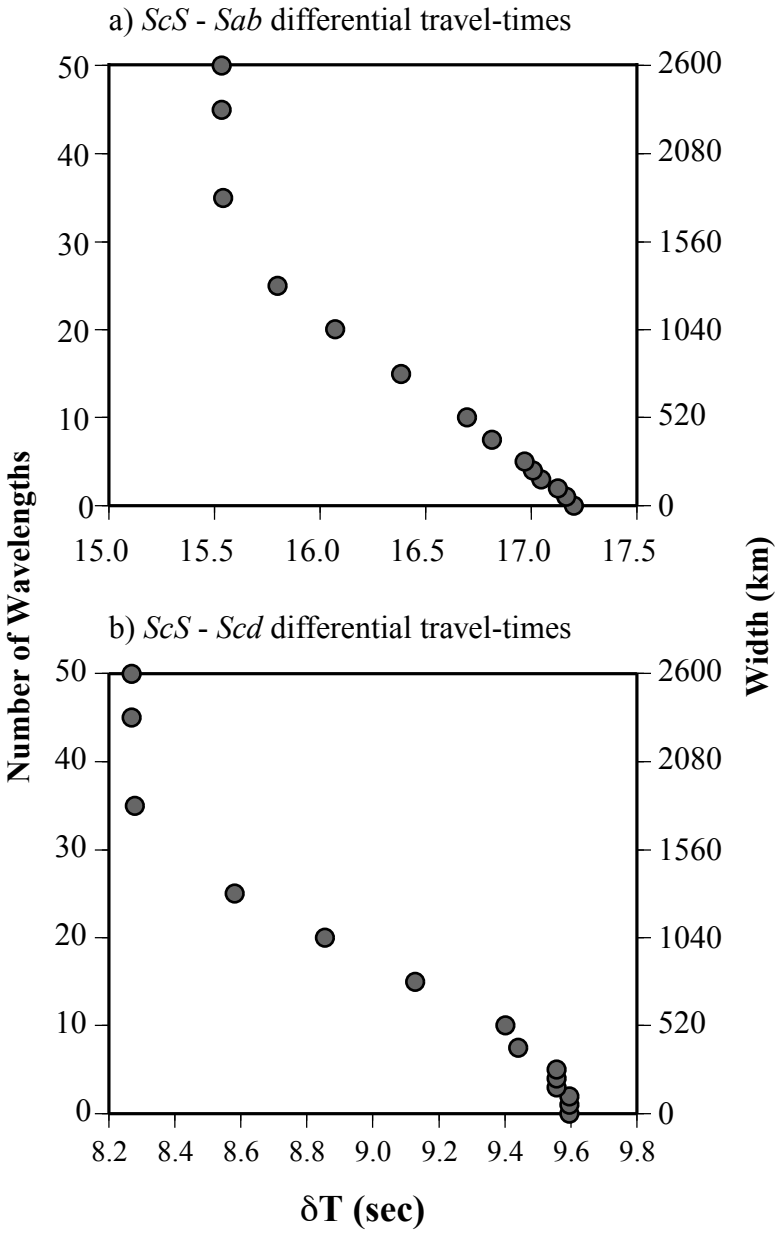

(Thorne, Lay, Garnero, Jahnke, and Igel. 2005)

(span one column; Black and White)

Figure 8.

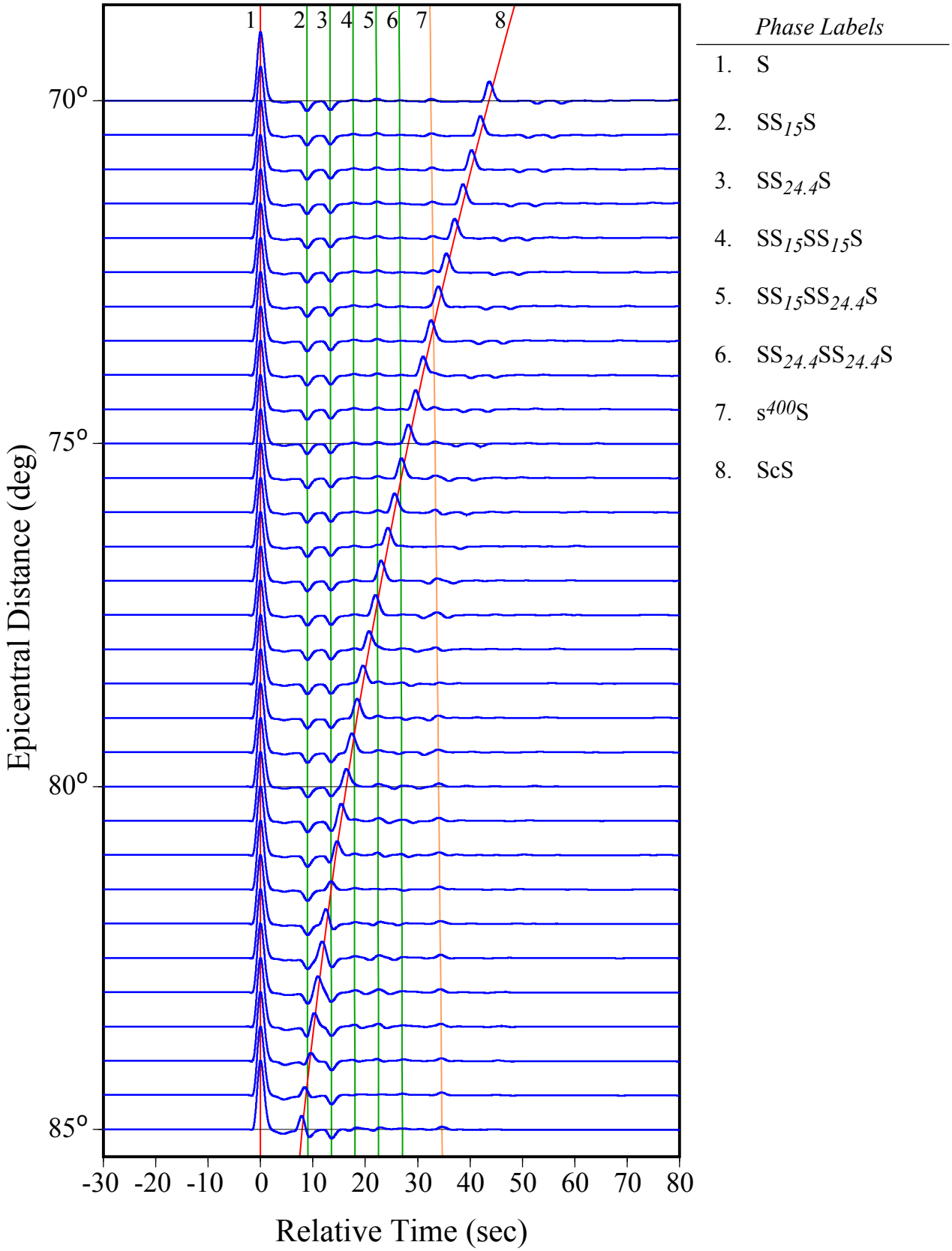

(Thorne, Lay, Garnero, Jahnke, Igel. 2005)

Supplement A.

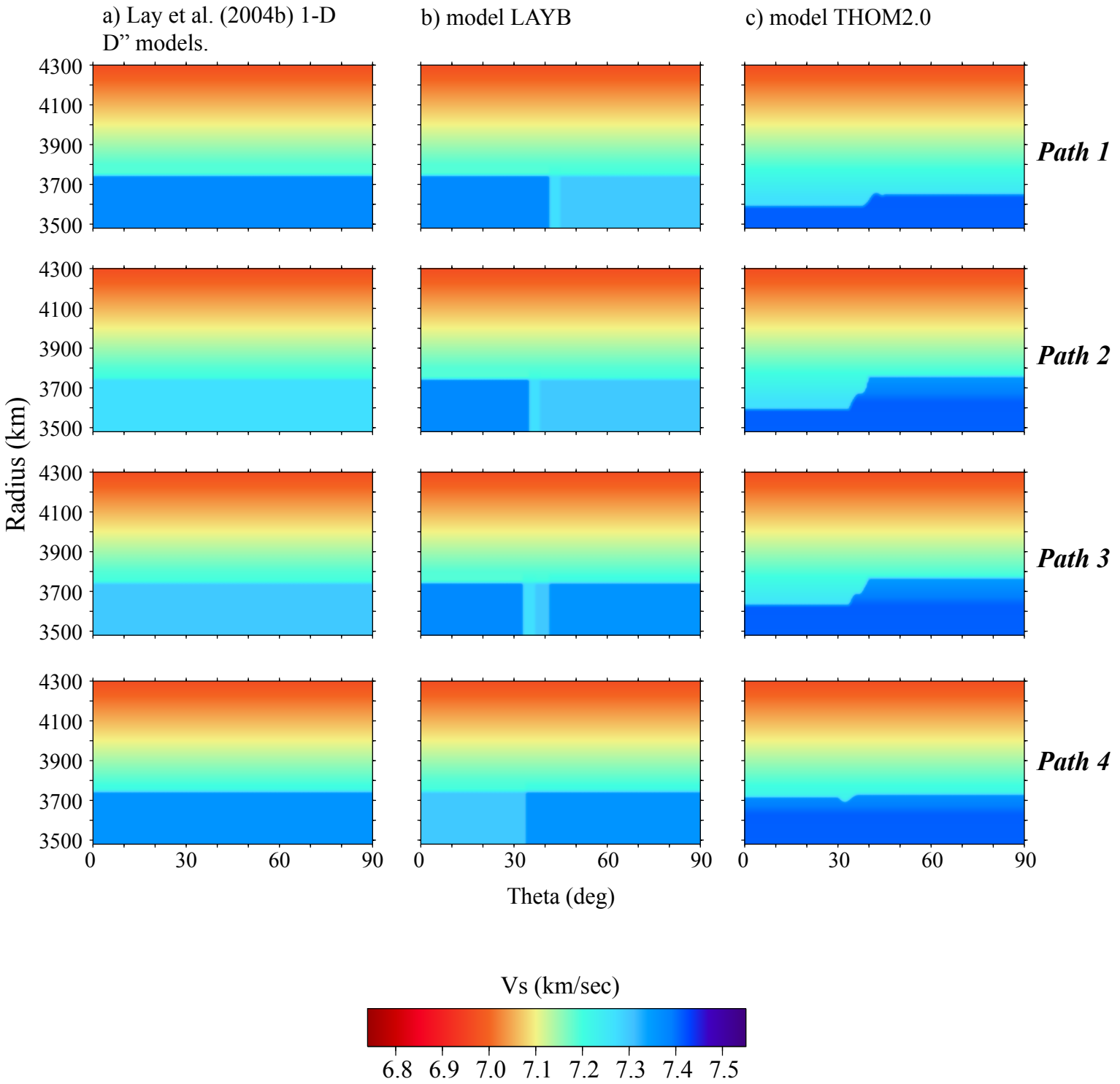

(Thorne, Lay, Garnero, Jahnke, Igel. 2005)

Supplement B.

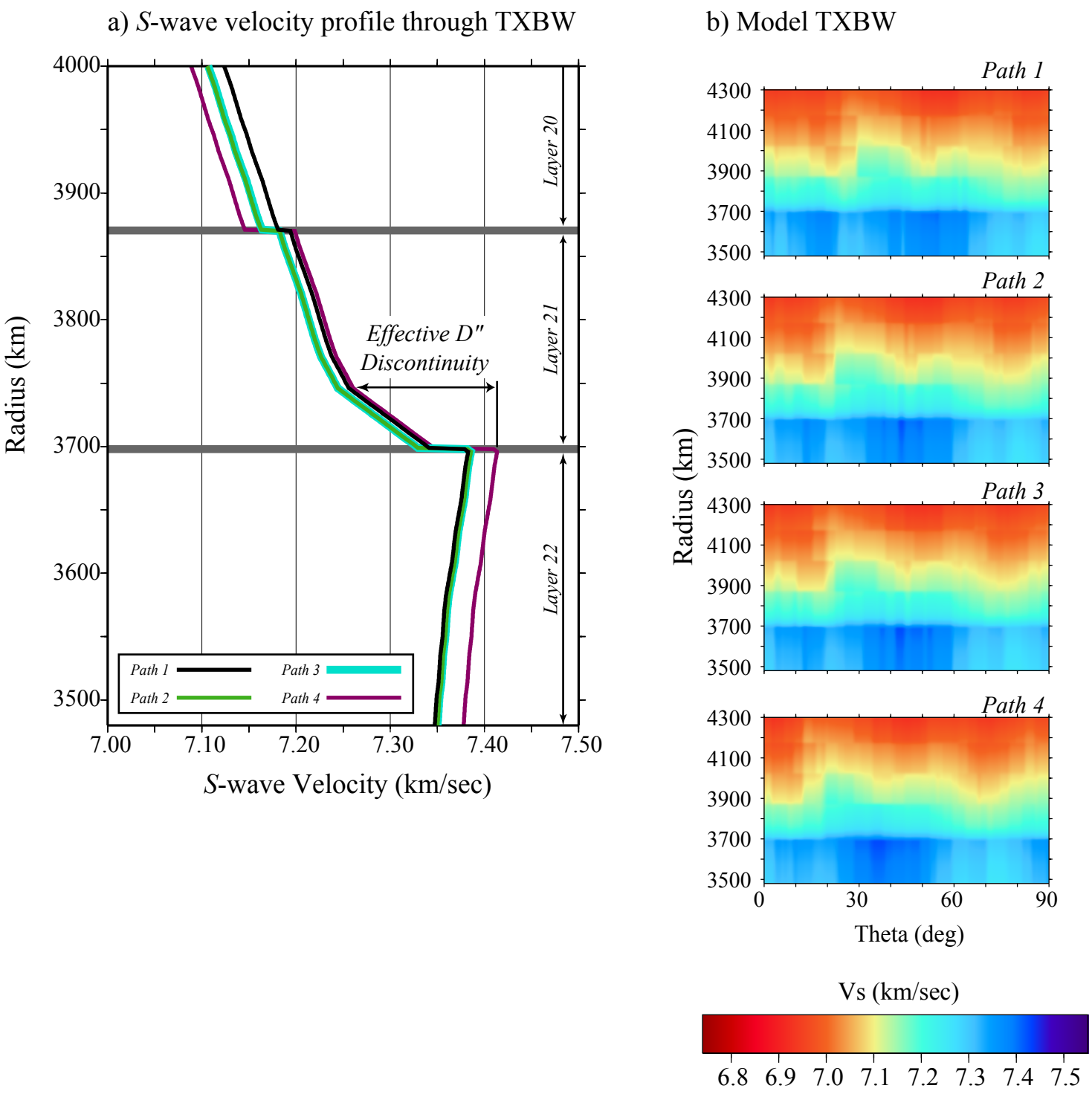

(Thorne, Lay, Garnero, Jahnke, Igel. 2005)

Supplement C.

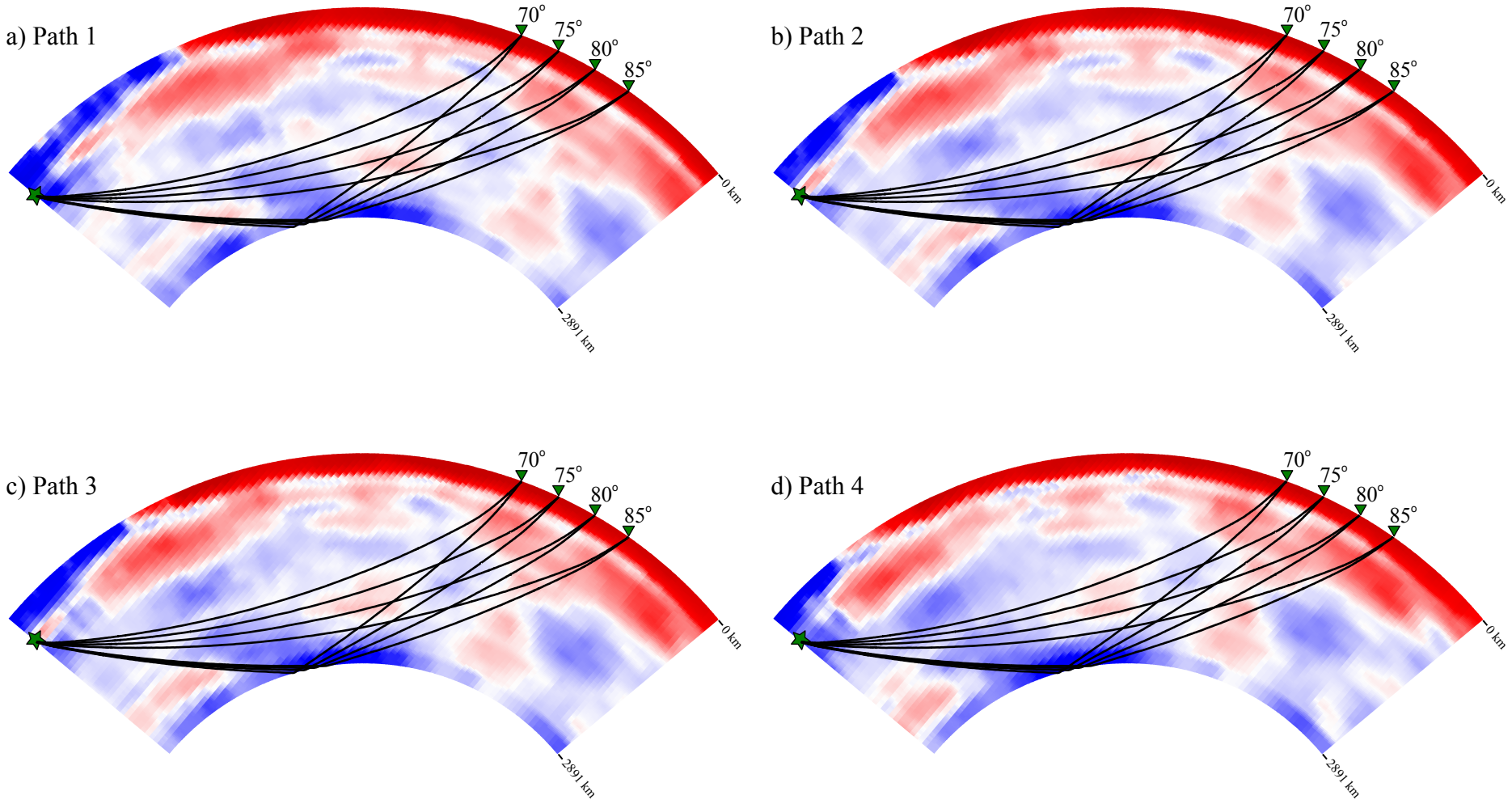

(Thorne, Lay, Garnero, Jahnke, Igel. 2005)

Supplement D.

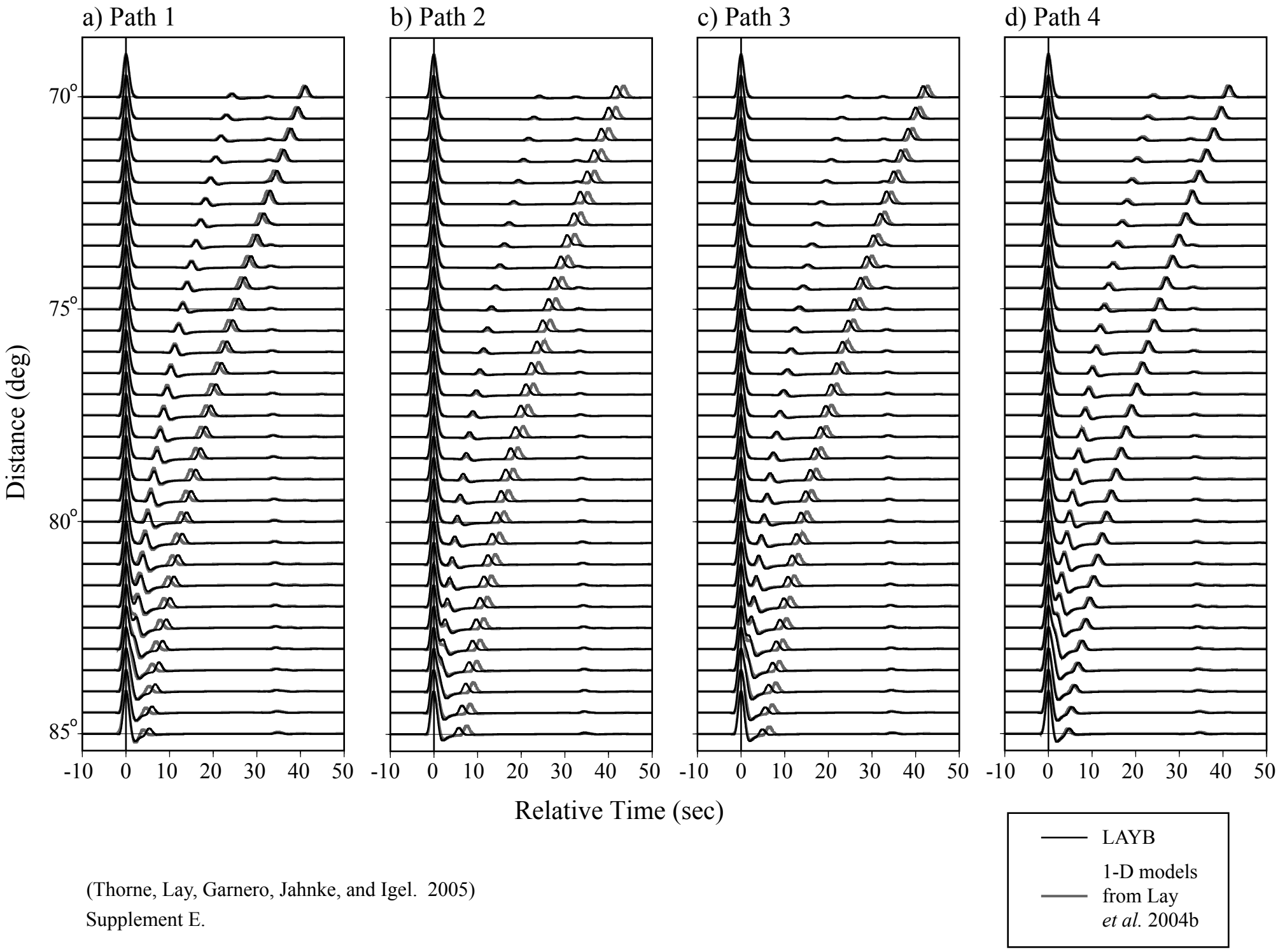

(Thorne, Lay, Garnero, Jahnke, and Igel. 2005)
Supplement E.

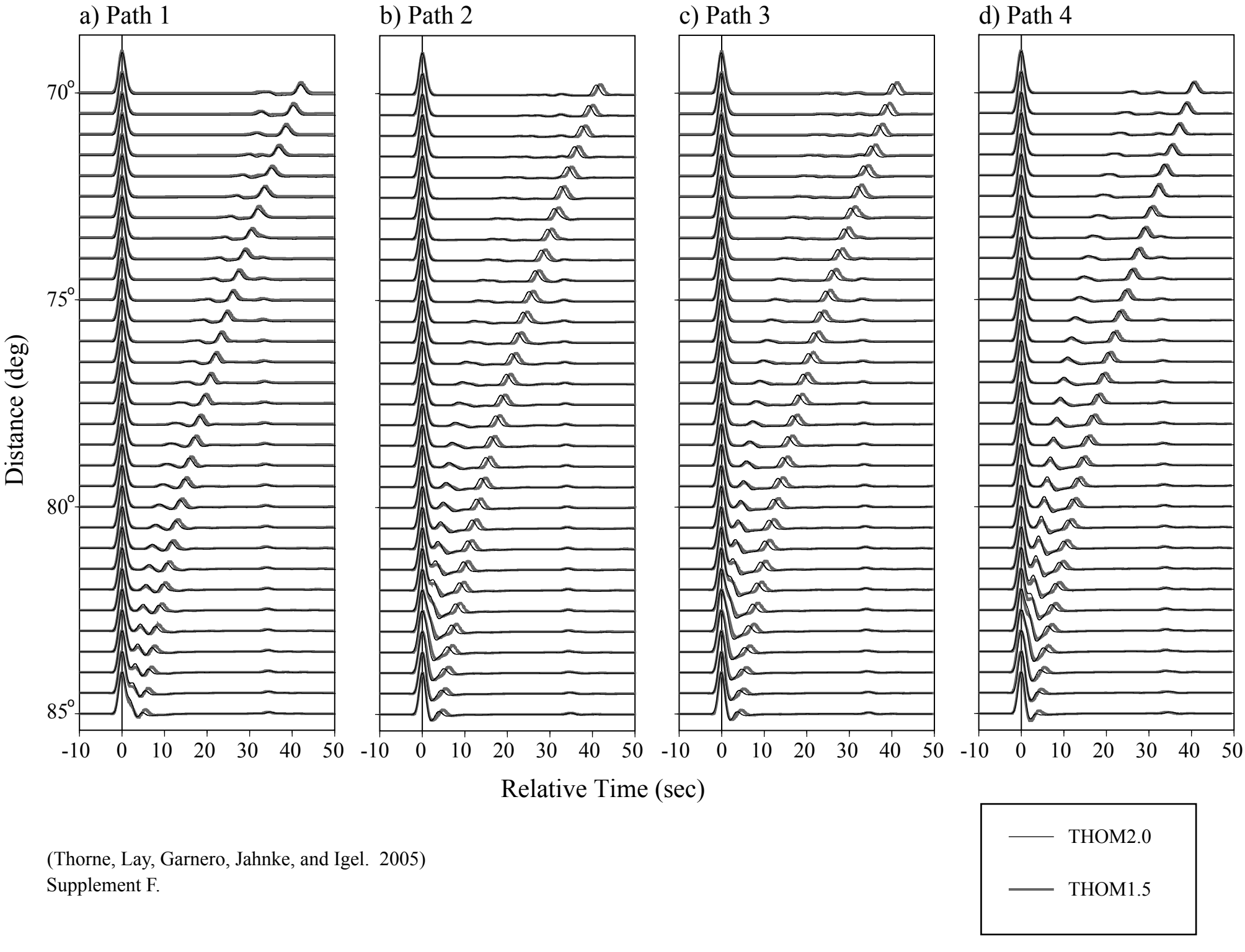

(Thorne, Lay, Garnero, Jahnke, and Igel. 2005)
Supplement F.